energies

MDPI

Article

Structural Architecture and Permeability Patterns of Crystalline Reservoir Rocks in the Northern Upper Rhine Graben: Insights from Surface Analogues of the Odenwald

Claire Bossennec [1,*], Lukas Seib [1], Matthis Frey [1], Jeroen van der Vaart [1] and Ingo Sass [1,2]

[1] Institute of Applied Geosciences, Geothermal Science and Technology, Technische Universität Darmstadt, Schnittspahnstraße 9, 64287 Darmstadt, Germany; seib@geo.tu-darmstadt.de (L.S.); frey@geo.tu-darmstadt.de (M.F.); vandervaart@geo.tu-darmstadt.de (J.v.d.V.); sass@geo.tu-darmstadt.de (I.S.)
[2] Helmholtz Centre Potsdam-GFZ German Research Centre for Geosciences, Telegrafenberg, 14473 Potsdam, Germany
* Correspondence: claire.bossennec@tu-darmstadt.de

Abstract: Fracture network is a crucial element to address in any model of the thermo-hydro-mechanical behaviour of a reservoir rock. This study aims to provide quantified datasets and a further understanding of the critical parameters of the fracture network pattern in crystalline rocks. In the Northern Upper Rhine Graben, such rock units are targeted for multiple energy applications, from deep geothermal heat extraction to heat storage. Eleven outcrops were investigated with a combined LiDAR and 2D profiles analysis to extract faults and fracture network geometrical parameters, including length distribution, orientation, connectivity, and topology. These properties are used to decipher the structural architecture and estimate the flow properties of crystalline units. Fracture networks show a multi-scale power-law behaviour for length distribution. Fracture topology and orientation are mainly driven by both fault networks and lithology. Fracture apertures and permeability tensors were then calculated for two application case studies, including the stress field effect on aperture. Obtained permeabilities are in the range of those observed in the subsurface in currently exploited reservoirs. The dataset provided in this study is thus suitable to be implemented in the modelling during the exploration stage of industrial applications involving fractured crystalline reservoirs.

Keywords: fracture network properties; discrete fracture network; flow properties; crystalline rock; faulted basement; geothermal reservoirs; heat storage reservoirs; structural analogues; Upper Rhine Graben

Citation: Bossennec, C.; Seib, L.; Frey, M.; van der Vaart, J.; Sass, I. Structural Architecture and Permeability Patterns of Crystalline Reservoir Rocks in the Northern Upper Rhine Graben: Insights from Surface Analogues of the Odenwald. *Energies* **2022**, *15*, 1310. https://doi.org/10.3390/en15041310

Academic Editor: Stefano Mazzoli

Received: 21 December 2021
Accepted: 7 February 2022
Published: 11 February 2022

1. Introduction

Geothermal energy and thermal energy storage are essential components of the balance required to ensure decarbonated energy supply by 2050. The Upper Rhine Graben (URG) is a targeted area for deep geothermal and heat storage projects since petrophysical rock properties of the faulted crystalline basement and the temperature field offer a high potential in the area [1–5]. Geothermal anomalies are not distributed homogeneously in the URG and are linked to lithological and structural changes [6,7]. Fault zones induce convective flows, thus increasing the temperature field heterogeneity.

Basin-scale studies show the importance of fault zones, in the compartmentalisation of fluid flow and control, on the architecture of a geothermal system in sedimentary and crystalline rocks [8–11]. However, datasets of quantified structural network properties and their local influence on flow properties within crystalline units are only sparsely available in the literature [12–16]. The petrophysical and geo-mechanical behaviour of crystalline rocks has been investigated in numerous studies at the sample scale in laboratory conditions [17,18]. Significant structures and lithological boundaries within the basement have been determined and modelled by geophysical methods [3,19,20]. Possible architectures of the fracture network and some conceptual models also exist [14,21–23]. In the area of interest, i.e., the Northern Upper Rhine Graben and its crystalline shoulders, some local studies characterise the fracture network at the outcrop scale in the granodioritic [15] and granitic basement [24]. However, the aim of integrating the local outcrops' structural analyses at the massif scale has not yet been achieved in this part of the URG and is a target of this study. The main limitations concern the quantification, before drilling wells, of the variability and heterogeneity of the fracture network in the crystalline basement and its impact on hydraulic behaviour at different depths. Semi-artificial Discrete Fracture Network (DFN) models [16,25–27] can be implemented here in a renewed approach to estimate the effect of fracture network heterogeneity, thus reducing uncertainty [28,29]. The semi-artificial character addresses here the variety of information extracted from the outcrops [30,31], with depth-modelled fracture variability. Indeed, at the exploration stage between seismic and drilling stages, the semi-artificial model workflow combines parametrised fracture datasets from field investigations, apertures estimations from different approaches [32–36], and geological studies *a priori* of the reservoir organisation in depth. These semi-artificial models help to give a first order view of the permeability range, thus increasing the transferability of outcrop analogues and derived conceptual models towards reservoir simulation.

This study aims to provide a near-surface analogue database of structural network properties, then establish a series of sub-surface semi-artificial DFN models. Two case studies are proposed to estimate the hydraulic behaviour of crystalline reservoirs in exploitation depths, with (1) an 800 m deep heat-storage reservoir (similar to that targeted in the project SKEWS [37–39]) and (2) a 4000 m deep-geothermal reservoir.

2. Geological Context

The European Cenozoic Rift System (ECRIS) was developed in Western Europe to respond to compressional intraplate stresses involved by the Pyrenean and Alpine orogens [40]. Several rift basins are part of the ECRIS, from North to South, the Lower Rhine Embayment, the Hessian Trough, the Upper Rhine Graben, the Bresse Graben, and the Limagne Graben. The Upper Rhine Graben (URG) is the central part of the ECRIS [41–44]. The Upper Rhine Graben is divided into three segments, e.g., the northern segment, the central segment and the southern segment [45,46]. In its northern part (NURG), the structural architecture of the basement is complex and structured by four units, from North to South, the Rhenohercynian Zone (RHZ), the Northern Phyllite Zone (NPZ), the Mid-German Crystalline High (MGCH), and the Saxo-thuringian Zone (STZ) [47,48] (Figure 1).

The NURG basement subunits expose a diversity of lithologies. The RHZ domain in the North is composed of Middle Devonian metamorphised paragenetic units [49]. Low greenschist facies metasediments and volcanic rocks form the NPZ [50,51]. Metamorphic and crystalline complexes from the MGCH constitute a significant part of the Northern URG basement. The MGCH is seen as the southern active continental margin of the subduction between Armorica and Laurussia [52,53]. The STZ comprises a Neoproterozoic gneiss basement [19,54]. This basement is overlain by low-grade metamorphised sedimentary and volcanic rocks deposited in a Cambrian-Devonian rift basin [3,19,55].

The Odenwald is the largest outcrop of the MGCH, valuable for investigating subsurface structural architecture. The MGCH represents a major part of the potential targets in the NURG. Thus, the Odenwald as an outcrop analogue is a good target for exploration workflow. Four units compose the Odenwald [54]: the Frankenstein Massif (Unit I); the Flasergranitoid zone (Unit II); the South Odenwald (Unit III), and the Böllsteiner Odenwald (Unit IV). Units I, II and III are grouped into the West Odenwald (also called Bergsträßer Odenwald), which is separated from the East Odenwald (Unit IV) by the N010° E striking Otzberg Fault Zone (OFZ). Unit I is composed of a paleo-volcanic arc and cadomian remnants [52], later intruded by gabbroic, granodioritic and granitic plutons during the Variscan orogeny [56,57]. Unit II is formed from the aggregation of genetically unrelated mafic and felsic granitoid intrusions [54,58]. The host-rock of Unit III is composed of amphibolite-facies metamorphosed metasediments, basites and gneiss, which were intruded by monzodiorite to granodiorite (Weschnitz pluton), granite (Tromm pluton) and gabbro to diorite with later granite and granodiorite intrusions (Heidelberg pluton) [59]. A Carboniferous sinistral strike-slip fault system delimits Unit I and Unit II [60]. The boundary between Unit II and Unit III is also marked by a sinistral strike-slip fault system [48], delimitating the Heppenheim Schieferzug meta-pelitic unit in the North and the Weschnitz granodiorite in the South [54]. The activation of the trans-tensive regime started in the Odenwald after the metamorphism and collision peak [48,53].

The variscan orogeny is subdivided into four steps [48]: D1 to D4. Compressional phases D1 and D2 initiated thrust sutures during the Variscan orogeny [48]. In the late Carboniferous, during the D3 phase, exhumation of the metamorphic rocks was accompanied by NE–SW sinistral shear zones involving plutonic intrusion emplacement. Normal faulting and NNE–SSW directed phase D4 expressed localised shear and fault zones and contributed to brittle deformation structures. D4 is also accompanied by the intrusion of dioritic to granitic magmas within this trans-tensive setting [58].

The Permian extension formed large intra-mountainous basins filled with coal and siliciclastics (e.g., Saar-Nahe, Lorraine) [61,62], and records the beginning of the basement weathering [63,64].

Basaltic and rhyolitic volcanic episodes (lamprophyres) alternate with Permian deposits [65,66]. Continuous subsidence affected the area from the Permian up to the Early Cretaceous [67,68]. This was followed by a regional uplift of the Rhenish Massif, at the NNW side of the URG, from Late Cretaceous to Paleocene, which eroded the sedimentary units down to the Lower Triassic and Permian units [45,69,70].

During the Cenozoic, the URG development, by passive rifting in the alpine foreland [40,41,71,72], reactivated variscan fault systems [45,46,73]. The initiation of the rift started in the Eocene, in response to the Alpine N–S compression. In the late Oligocene and Miocene, NE–SW directed systems were reactivated in a sinistral trans-tensive regime, with the maximal horizontal stress shifting from WNW to NNW orientation. During this new stress field phase, the depocenters drifted towards the NURG, while the southern URG uplifted, reactivating meanwhile NE to ENE striking faults [55]. The current stress field, active since the Pliocene, which affects the NURG, exhibits maximum horizontal stress striking N145° E [74]. This orientation leads to active subsidence and a trans-tensive regime in fault zones of the NURG [55,73–75]. Associated extensive and trans-tensive regimes induced local basaltic and trachytic volcanism (Kaiserstuhl, Vogelsberg) [60,76,77].

High-temperature anomalies tracing geothermal potential are linked to the stress field variability [6,7]. These anomalies are located preferentially in extensional shear and normal context, facilitating geothermal brine flow. Trans-pressive and uplift regimes dominate in the URG central segment, while trans-tensive and normal faulting prevail in the NURG at the boundary with the Odenwald [50,54,78].

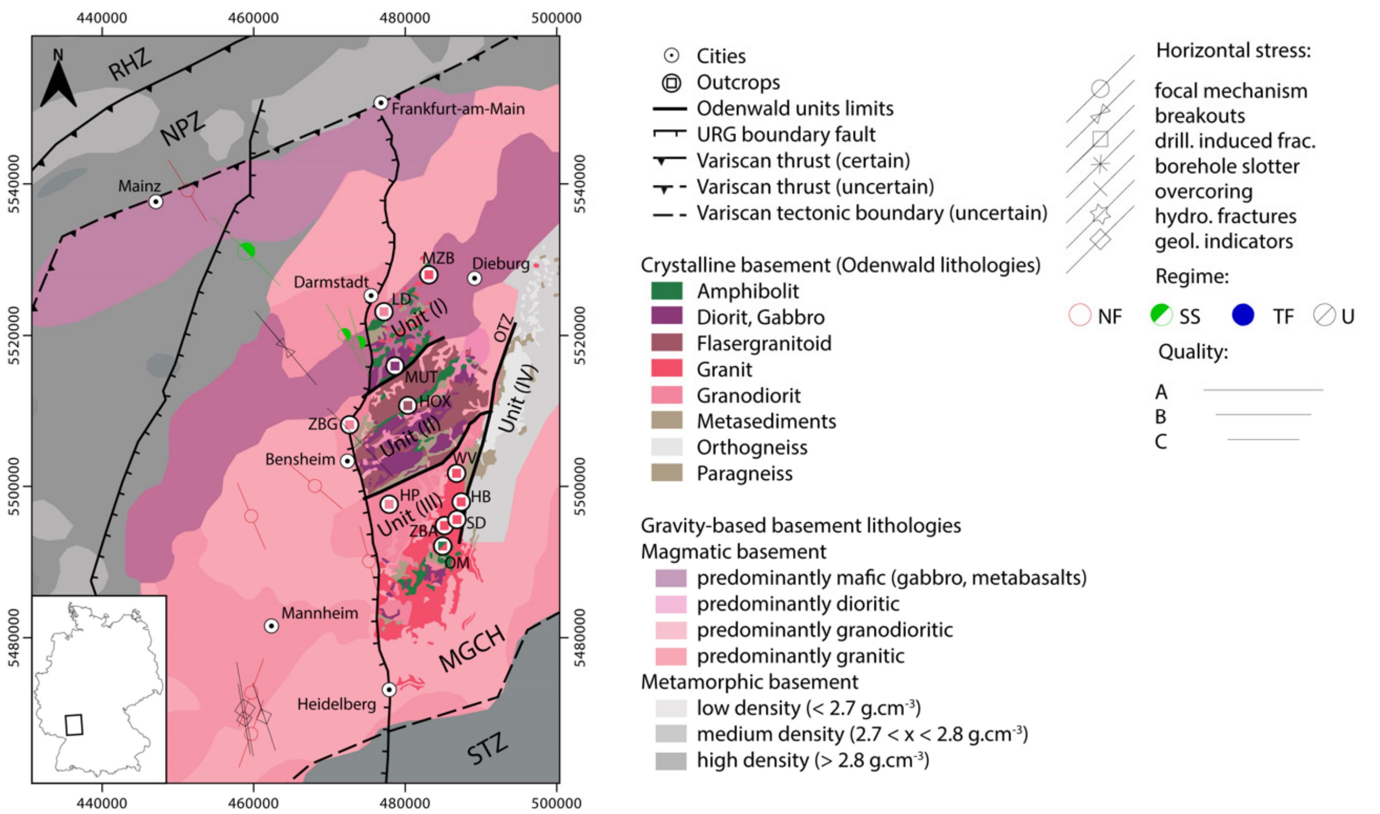

Figure 1. Geological map adapted from [79] for crystalline basement lithologies from the Odenwald, and [3] for lithological and tectonic boundaries based on the interpretation of the joint inversion of gravity and magnetics. Gravity and magnetics boundaries were extracted from [3], copyright Elsevier (2021). Outcrops are marked and colour coded according to their main lithology. Horizontal stresses are from [80]. Domain labelling: RHZ: Rheno-Hercynian Zone, NPZ: Northern Phyllite Zone, MGCH: Mid-German Crystalline High, STZ: Saxo-thuringian Zone, OTZ: Otzberg Fault system. Outcrops labelling: MZB: Mainzer Berg, LD: Lichtwiese, Darmstadt, MUT: Mühltal, HOX: Hoxhohl, ZBG: Zwingenberg, HP: Heppenheim, WV: Weschnitz valley, HB: Hammelbach, SD: Streitsdölle, ZBA: Zotzenbach, OM: Ober-Mengelbach.

3. Materials and Methods

In this study (Figure 1), a total of 11 locations involving 21 profiles were investigated to assess fracture network properties for an extensive range of lithologies and structural contexts (Figure 2, Table 1). The presented multi-disciplinary approach is divided into two main panels, which are (1) structural characterisation and (2) discrete fracture network (DFN) modelling to quantify flow patterns. The dataset includes a quarry investigation (Figure 2) at Mainzer Berg [15,81] and a structural study in the Tromm area [24,82], along with the newly acquired datasets from Lichtwiese, Mühltal, Hoxhohl, Zwingenberg and Heppenheim outcrops (Table 1).

3.1. Structural Data Acquisition and Treatment

At the regional scale, lineaments are investigated, using a DEM with 25 m and 5 m resolution (Figure 3). This regional analysis aims to extract length, orientation, density (number of lineaments per surface unit) and intensity (total lineament length per surface unit) (Table 2), following the workflow previously published in [12,13].

The chosen 11 outcrops exhibit the diversity of crystalline lithologies encountered in the Bergsträsser Odenwald. They also allow sampling in different structural contexts, from shearing fault systems to normal URG border faults (Figure 2).

Table 1. Sampling location and profile information, with number of items identified on LiDAR and digitised with GIS.

Location	UTM 32 Coordinates X	UTM 32 Coordinates Y	Main Lithology	Nb LiDAR Identified Planes	Profile ID	Profile Main Orientation	Nb GIS Digitised Items	Reference
Mainzer Berg (MZB)	483,094	5,528,012	Granite	1076	1 2 3 4 5	N010 N120 N120 N170 N095	542 414 1377 380 516	[15]
Lichtwiese, Darmstadt (LD)	477,176	5,523,147	Granodiorite	- -	1 2	N175 Horizontal plane	141 629	This study
Mühltal (MUL)	478,635	5,515,978	Gabbro	1197	1 2 3	N010 N150 N075	309 492 841	This study
Hoxhohl (HOX)	480,333	5,510,764	Flasergranitoid	572	1	N100	257	This study
Zwingenberg (ZBG)	472,627	5,508,186	Granodiorite	228	1	N090	413	This study
Heppenheim (HP)	477,885	5,497,621	Granodiorite	2212	1 2 3 4 5	N170 N080 N020 N080 N015	785 470 510 310 150	This study
Weschnitz (WV)	486,775	5,501,752	Granite	169	1	N090	1842	[24]
Hammelbach (HB)	487,401	5,497,948	Granite	159	1	N080	1351	[24]
Streitsdölle (SD)	486,817	5,495,632	Granite	456	1	N100	521	[24]
Zotzenbach (ZBA)	485,183	5,494,821	Granite	289	1	N130	1111	[24]
Obermengelbach (OM)	484,957	5,492,114	Amphibolite, Granite	1243	1 2 3 4	N150 N095 N150 N045	767 1647 2383 981	[24]

Table 2. Lineament analysis statistics, with dimension features, power-law parameters a, b, and r^2, and areal fracture density and intensity.

Layer	Min Length (m)	Max Length (m)	Mean Length (m)	a	b	r^2	P20 ($lin \cdot m^{-2}$)	P21 ($m \cdot m^{-2}$)
DEM 25 m regional (Figure 3a)	143	84,253	6247	4.09×10^{-3}	−1.41	0.98	5.74×10^{-8}	3.58×10^{-4}
DEM 25 m Odenwald (Figure 3b)	611	23,405	3419	1.07	−1.91	0.99	5.43×10^{-7}	1.86×10^{-3}
DEM 5 m Northern Odenwald (Figure 3c)	9	5606	845	2.06×10^{-1}	−1.69	0.99	5.77×10^{-6}	4.87×10^{-3}
DEM 5 m Southern Odenwald (Figure 3d)	50	5112	872	3.26	−2.2132	0.98	2.47×10^{-6}	2.16×10^{-3}

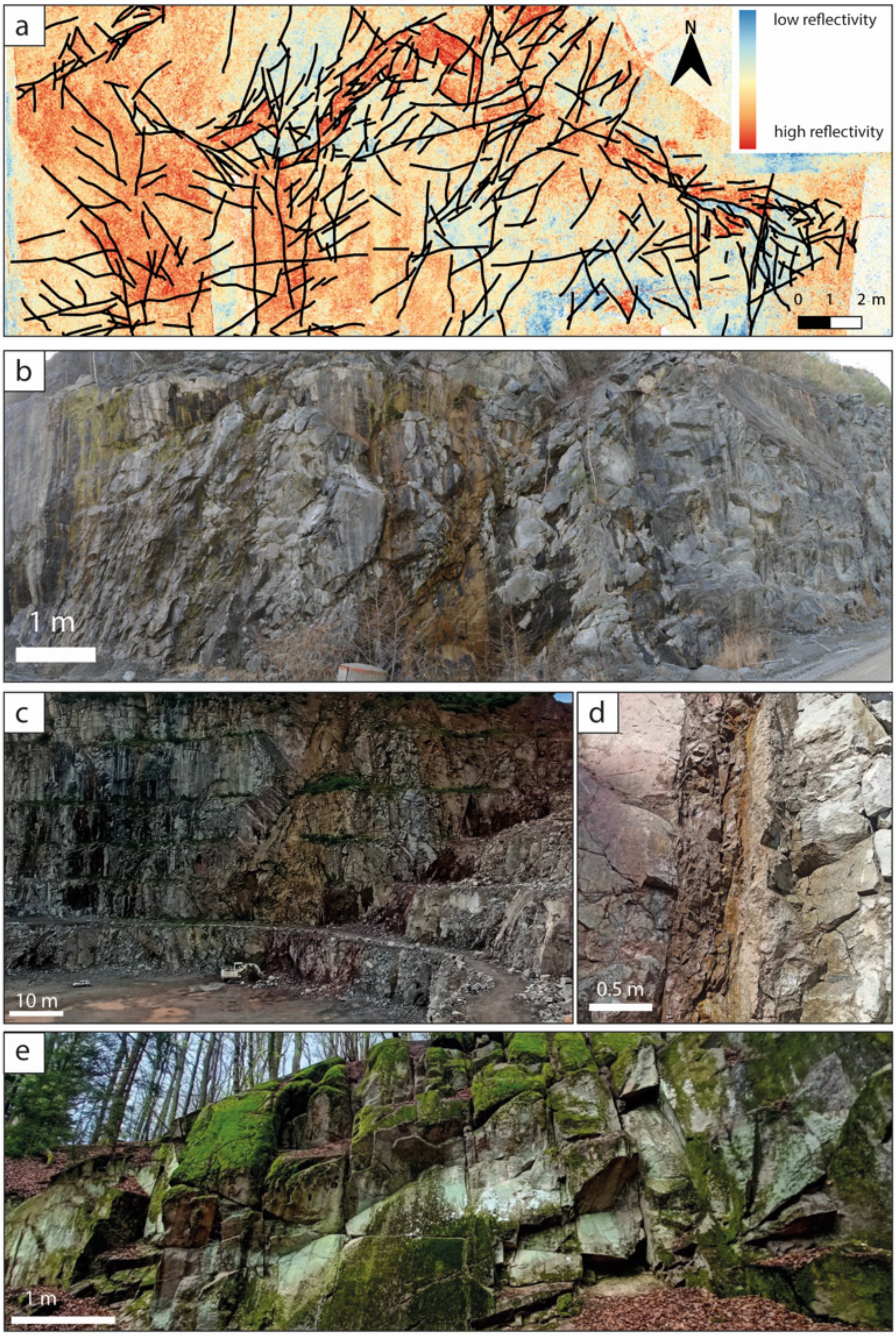

Figure 2. Field acquisition photographs targeted at specific lithologies and local structural context, (**a**) Fracture network outcropping at the top of the granodioritic pluton of Darmstadt, Unit I (Lichtwiese, Darmstadt). The background map shows the LiDAR reflectivity (**b**) Fault zone in the gabbroic unit of Unit I (Mühltal) (**c**) Fault zone related to the URG border fault system, in the granodioritic unit of the Weschnitz pluton, Unit III (Heppenheim) (**d**) Close-up of a secondary fault core in granodiorite (Unit III) (Heppenheim), (**e**) Fractured network in the Tromm granite, Unit III (Streitsdölle), in the vicinity of the Otzberg shearing fault system.

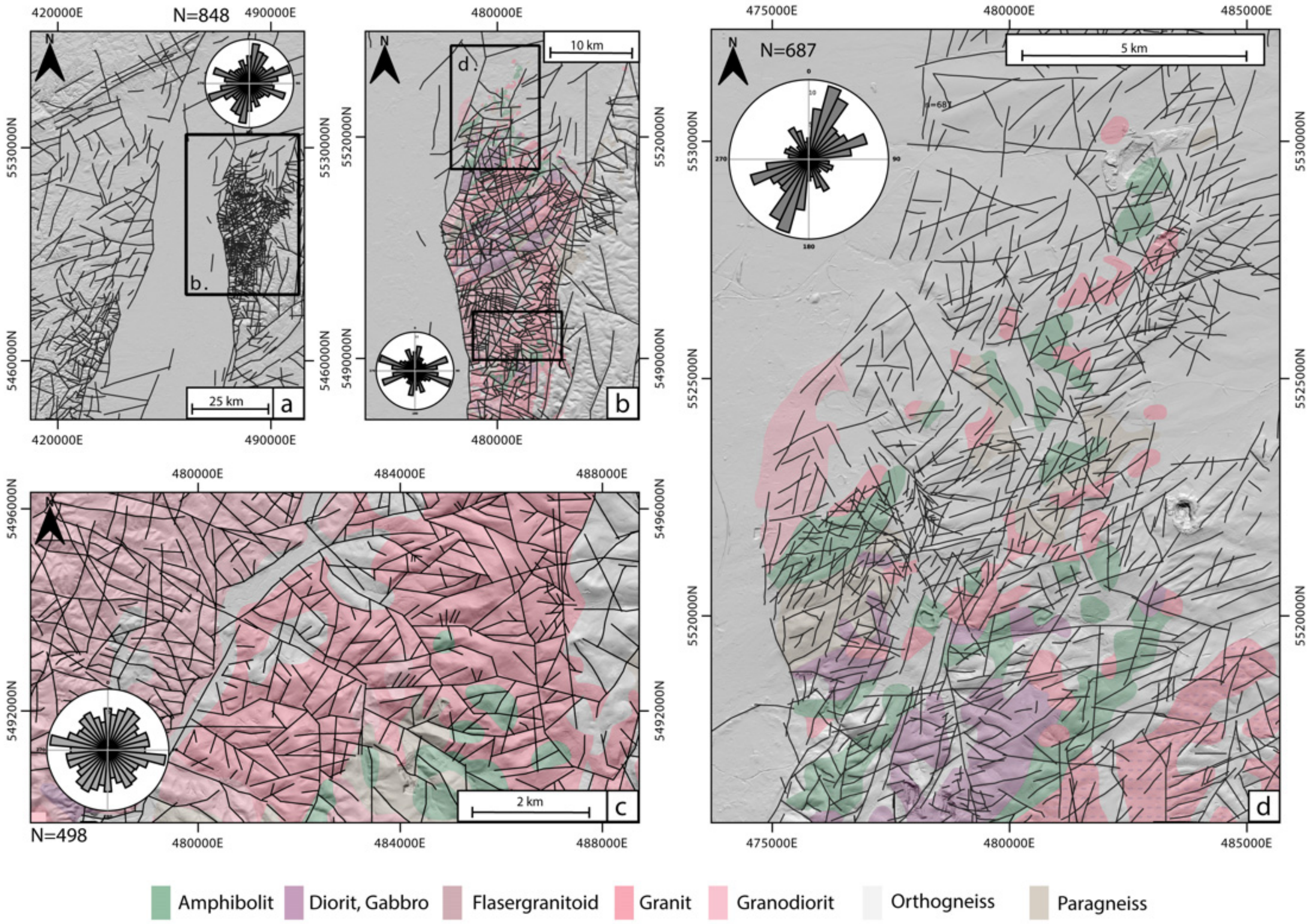

Figure 3. Lineament maps from the Northern URG, (**a**) 25 m resolution regional map, (**b**) close-up on the Odenwald, (**c**) 5 m resolution close-up of the southern Odenwald and (**d**) 5 m resolution close-up on the northern Odenwald [15]. For b, c and d; the colour code corresponds to the geological background and is adapted from [79] (see Figure 1 for the legend).

The description of field methods from a ground-based LiDAR and GIS acquisition methodology is similar to that used in a previously published study [15].

The LiDAR point cloud is oriented, normalised, and plane extraction from the Ransac [83] algorithm is applied. The obtained auto-recognised fracture planes are then analysed to extract their orientation. Plane dip directions are converted into strikes following the Left-Hand Rule.

The GIS interpretation is necessary to capture the apparent length, the topology of the fracture network and its potential clustering. Additionally, the GIS approach helps interpret fracture sets on outcrops with relatively flat surfaces (for instance, Lichtwiese pit walls) for which LiDAR workflow is not appropriate. For this purpose, the LiDAR data is rasterised via the SAGA cubic spline tool [84]. The rasters are then converted into hill shade layers, with N000° E, N045° E, N090° E, and N135° E orientation, to avoid misinterpretation of the lineament and fracture network, as explained in [12,13]. The following properties of the fracture network are extracted from GIS views (Table 3, Figures 4 and 5): length, orientation, linear density (P10), areal density (P20), areal intensity (P21), connectivity (C_L) [85], spacing (C_V) [86] and node topology [87,88]. The fracture clusters are extracted from the LiDAR and GIS analyses, with the input parameters for a stochastic distribution modelling, to be implemented in the DFN models (Tables 4 and 5).

Table 3. GIS Fracture network statistics, with dimension features, connectivity (C_L), power-law parameters a, b, and r^2, number of artificial scanlines ($N_{scanline}$), number of nodes per scanline (N_f), and spacing (C_v).

Locality	Profile n°	Area (m^2)	Nb Frac	Min Length (m)	Max Length (m)	Mean Length (m)	P10 ($frac{\cdot}m^{-1}$)	P20 ($frac{\cdot}m^{-2}$)	P21 ($m{\cdot}m^{-2}$)	C_L	*a*	*b*	r^2	$N_{scanline}$	Mean N_f	Mean C_v	Min C_v	Max C_v
MZB	1	610	414	0.48	13.90	1.97	1.32	0.68	1.34	2.06	1.13	−1.95	0.99	36	19.36	0.94	0.54	1.55
	2	129	542	0.17	4.73	1.01	3.03	4.20	4.24	1.53	1.06	−1.71	0.99	36	4.00	0.92	0.59	1.41
	3	400	1377	0.04	11.68	1.01	3.05	3.44	3.48	2.82	1.12	−1.55	0.99	7	56.71	0.93	0.67	1.41
	4	3870	380	1.02	32.58	5.23	0.44	0.10	0.51	2.55	0.71	−1.87	1.00	12	28.67	1.10	0.74	1.89
	5	2525	516	0.50	33.47	4.22	0.76	0.20	0.86	2.78	0.27	−1.95	0.99	17	30.41	1.00	0.54	1.29
LD	1	44	141	0.11	5.12	0.94	2.05	3.20	3.02	3.78	1.04	−1.51	0.97	14	27.36	1.02	0.65	1.91
	2	375	629	0.01	8.46	1.18	3.06	1.68	1.98	3.45	0.72	−1.43	0.99	10	13.20	0.94	0.61	1.26
MUL	1	745	309	0.62	16.86	3.00	1.29	0.41	1.24	5.37	0.61	−1.37	0.99	12	23.92	0.94	0.72	1.22
	2	2926	492	0.17	23.81	5.26	0.77	0.17	0.88	4.48	0.38	−1.13	0.97	13	44.62	0.98	0.51	1.39
	3	3278	841	0.55	48.92	3.96	0.76	0.26	1.01	4.74	0.52	−1.40	0.99	16	39.25	0.94	0.77	1.20
HOX	1	238	257	0.34	11.30	1.72	1.77	1.08	1.86	5.39	0.63	−1.02	0.97	14	21.64	1.00	0.68	1.49
ZBG	1	920	413	0.21	14.89	2.33	0.85	0.45	1.05	2.44	0.40	−1.17	0.97	17	23.00	1.13	0.66	1.67
HP	1	885	785	0.16	13.34	2.26	1.41	0.89	2.01	2.01	1.23	−1.69	0.99	14	42.07	1.00	0.74	1.43
	2	1233	470	0.75	36.23	4.15	0.80	0.38	1.58	5.64	1.36	−2.00	0.99	17	37.29	0.89	0.68	1.14
	3	3289	510	0.40	13.19	2.30	0.80	0.16	0.36	5.59	0.43	−2.30	0.99	23	23.26	0.93	0.64	1.22
	4	454	310	0.24	13.25	1.85	1.53	0.68	1.26	4.56	0.92	−1.69	1.00	29	25.90	0.91	0.58	1.41
	5	14,798	150	4.60	49.26	16.82	0.15	0.01	0.17	4.45	0.29	−1.57	0.99	19	15.26	0.79	0.55	1.19
WV	1	119	1842	0.03	7.57	0.81	6.02	15.48	12.54	4.09	2.02	−2.11	1.00	28	46.25	1.09	0.69	2.40
HB	1	67	1351	0.03	3.91	0.54	7.74	20.16	10.89	3.94	1.62	−2.34	1.00	30	42.53	0.88	0.64	1.55
SD	1	288	521	0.06	12.96	1.57	2.23	1.81	2.84	3.44	0.92	−1.48	0.99	28	24.11	0.98	0.57	2.21
ZBA	1	475	1111	0.10	11.22	1.28	1.98	2.34	2.99	2.96	1.28	−2.54	1.00	29	31.14	1.04	0.77	1.61
OM	1	200	973	0.05	7.27	0.98	2.65	4.87	4.77	3.02	1.08	−1.80	0.99	20	31.20	0.91	0.67	1.17
	2	300	1981	0.06	6.24	0.89	3.26	6.60	5.88	3.11	1.38	−1.91	0.99	33	48.27	0.93	0.53	1.40
	3	250	2895	0.02	7.74	0.62	4.00	11.58	7.18	3.30	1.07	−2.20	1.00	31	52.13	0.98	0.65	1.54
	4	300	1280	0.06	10.28	1.10	2.50	4.27	4.69	3.43	1.12	−1.75	0.99	36	30.61	1.05	0.70	1.79

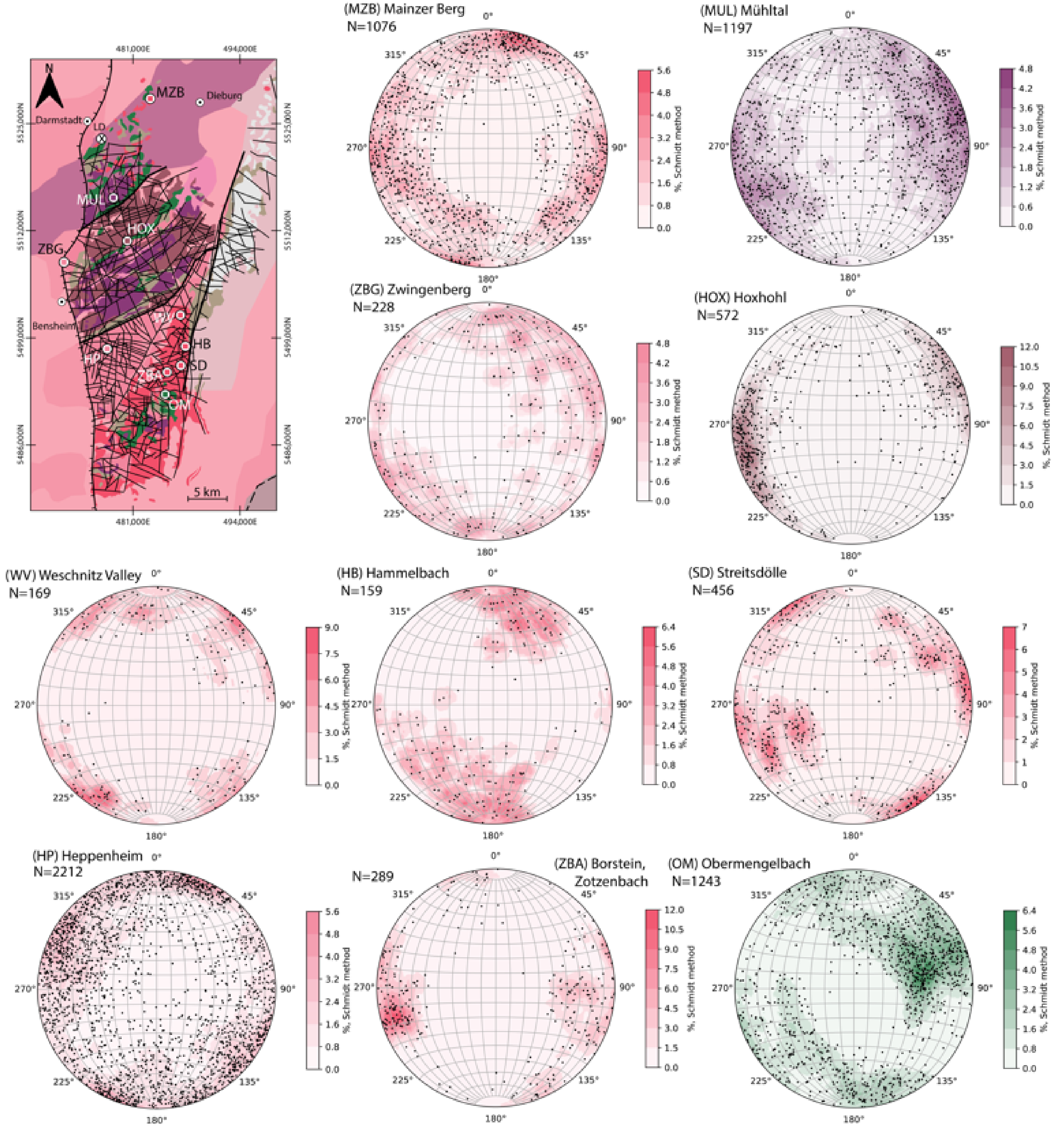

Figure 4. Orientation of the fracture network from outcrops with the mini-map, with outcrop location and Schmidt canvas with lower hemisphere projection stereograms. The applied colour code is related to the particular host lithology (see Figure 1).

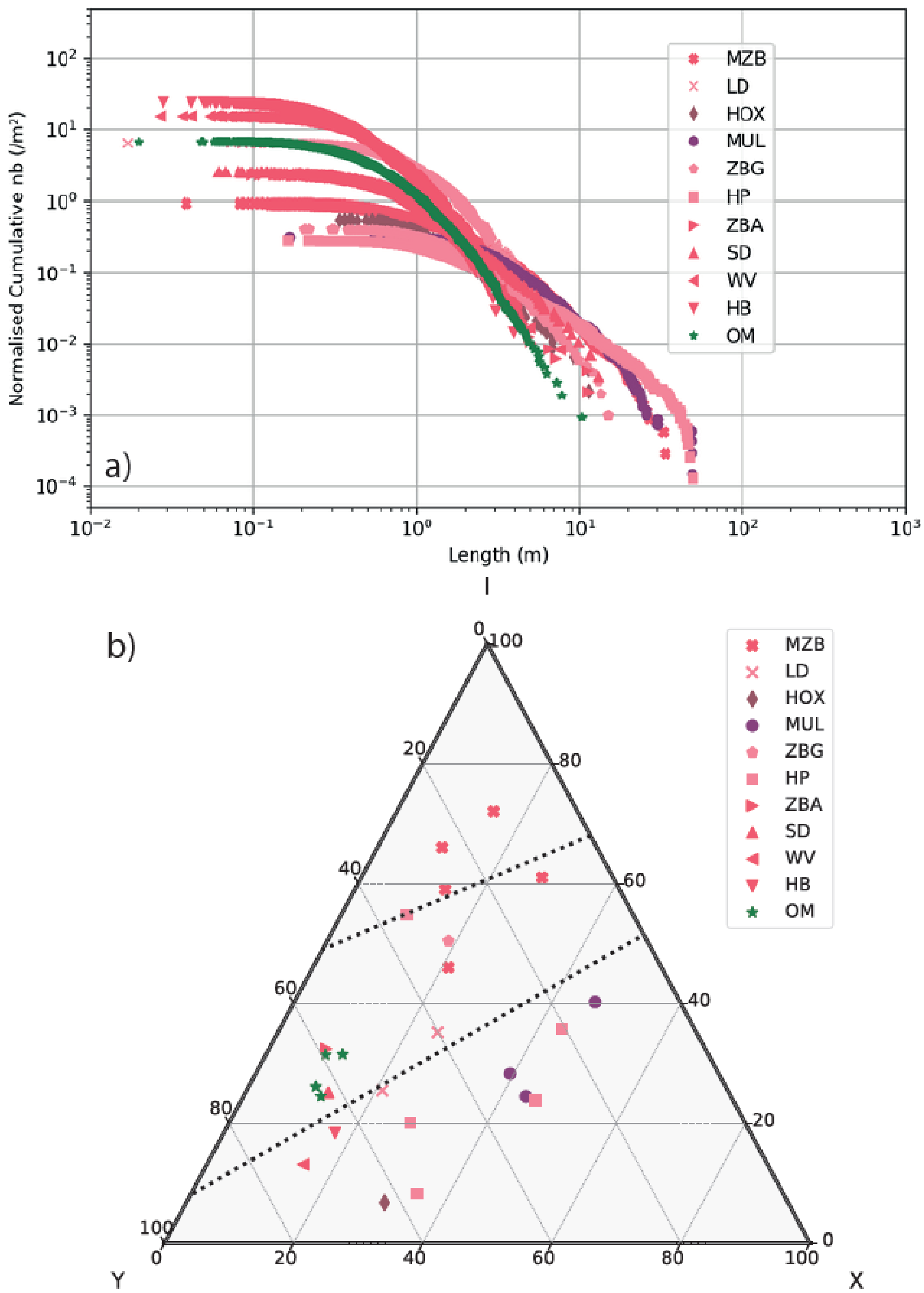

Figure 5. Fracture network features from 2D profiles and maps: (**a**) Cumulative distribution of fracture lengths from GIS analysis, (**b**) Connectivity ternary diagram. The applied colour code is related to the lithology (see Figure 1). For the list of abbreviations, see Figure 4 and Table 1. Outcrops labelling: MZB: Mainzer Berg, LD: Lichtwiese, Darmstadt, MUL: Mühltal, HOX: Hoxhohl, ZBG: Zwingenberg, HP: Heppenheim, WV: Weschnitz valley, HB: Hammelbach, SD: Streitsdölle, ZBA: Zotzenbach, OM: Ober-Mengelbach.

Table 4. Fracture network cluster inputs selected for the stochastic DFN models simulated.

Model	Cluster name	Global P10 (frac·m^{-1})	Trend	Plunge	a95	a99	kappa	P10
LD (Case 1)	1	3.06	33.9	16	2.2	2.7	30.4	1.03
	2	3.06	99.4	14.3	2	2.4	52.7	0.71
	3	3.06	132.6	15.4	2	2.5	64.7	0.54
	4	3.06	345.1	16.3	2.1	2.6	44.1	0.77
HP (Case 2)	1	1.53	199.4	13.8	14.5	18.2	4.4	0.48
	2	1.53	130.4	18.5	4.6	5.8	25.2	0.66
	3	1.53	307.6	8.8	6.1	7.6	26	0.38

Table 5. Model features parametrisation, with fracture law used, and associated parameters, fracture clusters name (for fracture cluster properties, see Table 4), termination (with (x) or without (o)), percentage of open fracture considered, and aperture parametrisation (with (x) or without (o) shear-dependent aperture).

Model	Model nb.	Fracture Law	Fracture Clusters	Termination	% Open Fractures	Shear Dependent Aperture
LD (case 1)	9	powerlaw (2,2)	LD1, LD2, LD3, LD4	o	100	x
	12	powerlaw (2,2)	LD1, LD2, LD3, LD4	o	100	o
	3	powerlaw (2,2)	LD1, LD2, LD3, LD4	x	100	o
	8	powerlaw (2,2)	LD1, LD2, LD3, LD4	o	100	x
	10	powerlaw (2,2)	LD1, LD2, LD3, LD4	x	10	x
	4	powerlaw (2,2)	LD1, LD2, LD3, LD4	o	10	o
	5	powerlaw (2,2)	LD1, LD2, LD3, LD4	o	10	x
	2	powerlaw (2,2)	LD1, LD2, LD3, LD4	x	10	o
	7	powerlaw (2,2)	LD1, LD2, LD3, LD4	x	1	x
	6	powerlaw (2,2)	LD1, LD2, LD3, LD4	o	1	o
	11	powerlaw (2,2)	LD1, LD2, LD3, LD4	o	1	x
	1	powerlaw (2,2)	LD1, LD2, LD3, LD4	x	1	o
	13	deterministic	-	-	100	o
	14	deterministic	-	-	100	x
HP (case 2)	1	powerlaw (2,2)	HP1, HP2, HP3	o	100	x
	2	powerlaw (2,2)	HP1, HP2, HP3	o	100	o
	3	powerlaw (2,2)	HP1, HP2, HP3	x	100	o
	4	powerlaw (2,2)	HP1, HP2, HP3	x	100	x
	5	powerlaw (2,2)	HP1, HP2, HP3	o	10	x
	6	powerlaw (2,2)	HP1, HP2, HP3	o	10	o
	7	powerlaw (2,2)	HP1, HP2, HP3	x	10	x
	8	powerlaw (2,2)	HP1, HP2, HP3	x	10	o
	9	powerlaw (2,2)	HP1, HP2, HP3	o	1	o
	10	powerlaw (2,2)	HP1, HP2, HP3	x	1	o
	11	powerlaw (2,2)	HP1, HP2, HP3	o	1	x
	12	powerlaw (2,2)	HP1, HP2, HP3	x	1	x
	13	deterministic	-	-	100	o
	14	deterministic	-	-	100	x

3.2. DFN Properties Modelling from the Near-Surface Dataset

DFN models presented in this study were generated using the FracMan software. Such DFN models aim to integrate the fracture network properties estimated on outcrops and upscale these to quantify the hydraulic properties of the fractured crystalline basement in sub-surface conditions [27,30–32].

The fracture generation follows the DFN workflow in the FracMan software [89]. Two cases studies were implemented (Figure 6a,b), with (1) a heat-storage test site at 800 m depth in the granodiorite below Lichtwiese (LD); and (2) a deep geothermal faulted reservoir at 4000 m within a granitic body in the NURG. Previous studies in crystalline rocks [9,56–58] have suggested that natural fracture networks are mineralised to a large extent at reservoir depth, thus reducing fluid flow. Three ratios of effectively opened fractures are therefore tested (1, 10 and 100%) [24]. Stochastic DFN is modelled in a 150 * 150 * 50 m box, as the input dataset does not provide enough information to implement vertical heterogeneity. For case (1), fracture orientations are extracted from the GIS map of the LD horizontal surface outcrop (Table 4), assuming a similar organisation in the subsurface, 800 m below. For case (2), fracture orientations and length distribution are extracted from the Heppenheim outcrop (Table 5) and modelled for a depth of 4000 m to represent a deep geothermal granodioritic reservoir, by applying a related vertical stress field. Each fracture cluster is parametrised following the Levy Lee generation model [90] and calibrated with the average P10 extracted from the GIS analysis. Fracture orientation follows a Fisher distribution [91]. A random seed number is reinitiated at each realisation. The fracture length distribution was set according to the computed power law, with a coefficient of −2.02, l_{min} of 1 m and l_{max} of 50 m. Aperture was parametrised (a) as fracture length-dependent, following the relation a = FractureRadius (m) × 10^{-6} [21], and (b) as shear dependent. For this second scenario of aperture estimation, a regional pattern with highest principal stress σ_1 and vertical and extensive σ_3 oriented N145° E [74,92] is considered. For the two case studies, the far-field regional stress field is implemented from [92] for depths of 800 m and 4000 m. The effective stress magnitude of the fracture plane is calculated following Mohr-Coulomb criteria [32], with the cohesion of 28 MPa [93] and pore pressure of 20 MPa for case (1), and 80 MPa for case (2). The resulting stress magnitude is integrated into fracture aperture estimation [32,94], following linear elastic fracture mechanics (Equation (1)) [95].

$$a = \sqrt{L}\frac{K_c\left(1-\nu^2\right)}{E\sqrt{\pi/8}} \quad (1)$$

where a is the fracture aperture, ν, the Poisson Ratio, E the Young Modulus, L the fracture radius and Kc the fracture toughness, dependent on the maximum stress.

The fractured rock is considered as an anisotropic porous medium, in which the rock matrix is parametrised as impermeable, and those flow pathways are restrained to connected fractures. The permeability of each fracture (k_f) is determined by cubic law of the aperture [96], following Equation (2).

$$k_f = \frac{a2}{12} \quad (2)$$

The equivalent permeability tensor is then calculated for each DFN model, following the Oda approach [97]. Permeability tensors are calculated in a regularly spaced grid, with a cell size of 0.8 × 0.8 × 0.625 m. Such cell size allows modelling of the properties of high-intensity fracture clusters and thus quantification of their impact on permeability at a metric scale.

Additionally, for the two case studies, deterministic DFN models were implemented (Figure 6c), in which matrix permeability is fixed with a normal distribution of $10^{-18} \pm 1.10^{-19}$ m^2. The fracture aperture is parametrised with the two approaches, identical to those applied for stochastic DFNs.

The use of outcrop datasets to estimate rock properties from DFN is potentially affected by several uncertainties. Following the work of [98], uncertainties can be categorised into three types, applicable to DFN:

Type (1) Measurement errors due to faulty observations, imprecision and bias.

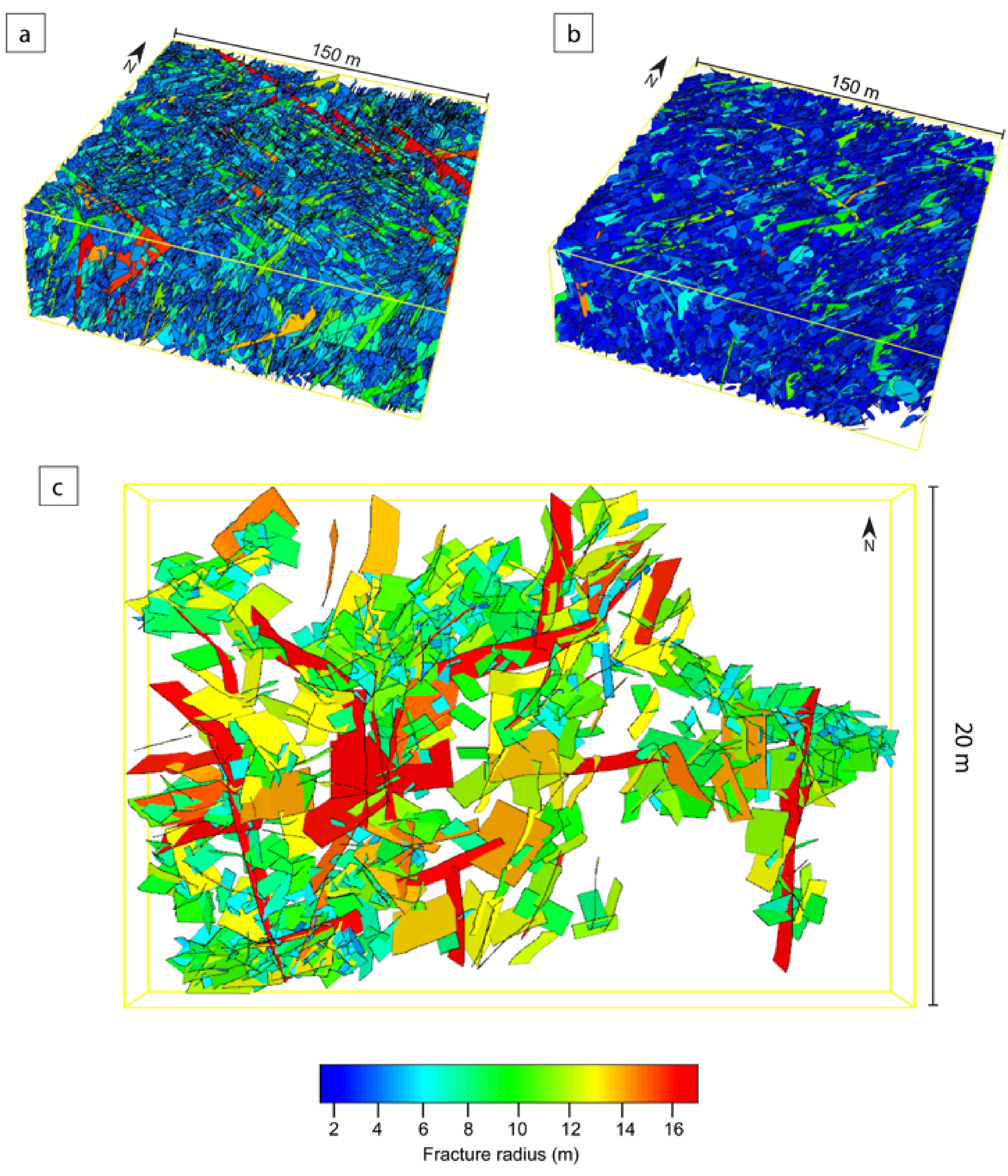

Figure 6. Semi-artificial DFN models, (**a**) Case n°1: Heat-storage purpose (800 m depth in a granodioritic unit), (**b**) Case n°2: Deep-geothermal faulted granitic reservoir (4000 m), (**c**) deterministic model for case 1.

This first category issues from limitations of the measurement devices in accuracy and precision in both detection and output. Uncertainty from mis-observations in reading measurements and detecting data, like simply missing a fracture, is also included in category 1. Bias, including over- and underestimation, also falls under this type of uncertainty. These uncertainties can usually be reduced by acquiring new data or improving the measurement devices [29]. For instance, here there is a possibility that the number of fractures is overestimated at the surface, due to weathering and mining processes, hence the interest in comparing to subsurface data.

Type (2) Variability and stochasticity. This uncertainty is related to the description of the natural heterogeneity seen in geological features [28]. Geostatistical methods and processes limit these types of uncertainty. The uncertainties can be estimated through, for instance, data relationship analysis and (stochastic) interpolation [98,99].

Type (3) Knowledge gaps, simplifications and ignorance. This uncertainty is impossible to quantify because it is based on unknown or non estimated information [100]. For instance, to transfer the DFN from near-surface to deep subsurface conditions, a local stress field that has not been recorded may change the nature of the fractures altogether. Whilst type 3 errors are impossible to reduce, type 1 and type 2 uncertainties can be limited by additional data and analysis.

4. Results

4.1. Structural Pattern of the Northern URG

Four lineament strikes dominate the structural trend of the NURG, i.e., N000–N015° E, N050–N075° E, N100–N115° E and N150–N165° E (Figure 3a). The same orientations characterise the Odenwald itself. However, lineaments striking N100–N115° E and N055–N070° E are in a dominant proportion, compared to N000–N015° E and N150–N165° E, contrary to the regional trend (Figure 3b). Within the Odenwald, the major strike also varies locally. The granitic and granodioritic southern Odenwald, previously investigated for the Tromm pluton by [24], mainly exhibits lineaments oriented N100° E, and three wider groups oriented NNE–SSW, ENE–WSW, and NNW–SSE (Figure 3c). The Northern Odenwald (Unit I, Figure 3d), regionally investigated by [15], is affected mainly by lineaments trending N010–N025° E, N055–N070° E and N150–N165° E. Lineaments striking N110–120° E are also observed but in a smaller proportion than in the Odenwald pattern.

Table 2 summarises the lineaments' geometrical statistics from the regional study. The power–law slope parameter b ranges from −1.41 to −2.2 and increases with the analysed resolution.

4.2. Fracture Network Patterns and Their Structural Context

Several patterns of fracture network architecture were observed in the field and by LiDAR imaging (Figures 1, 2 and 4). Involving multiple clustering levels, presence of normal and shearing fault zones, fracture infills and mineralised fault cores, the dataset covering these 11 outcrops exhibits the diversity of structures that may be encountered in the Odenwald massif within the vicinity of large shearing and normal fault zones. In Mainzererg, the granodiorite is characterised by an enhanced heterogeneity of fracture intensities around weathered fracture and fault corridors [15]. At Lichtwiese (LD), the outcrop exhibits a complex fracture at the top of the granodioritic pluton (Figure 2a). This outcrop is located near the discordance separating the granodioritic basement (Unit I) from Permian sediments (belonging to the Sprendlinger Horst on the East). This discordance might be a fault zone, but further investigations are required. In Mülhtal (MUL), gabbroic intrusion, oriented mainly NE–SW, exhibits fault zones with clay infill and a fault damage zone, with thicknesses from 1 to 10 m and oriented NNW–SSE and NNE–SSW (Figure 2b). Several of the fracture corridors within the fault damage zone exhibit cataclasis. In Zwingenberg (ZBG), located near the URG border fault oriented N010–N020, the granodiorite outcrop presents an excellent example of a background fracture network which affects crystalline rocks in the vicinity of a large fault zone. In Hoxhohl (HOX), the flaser-granitoid outcrop also exhibits background fracturing affecting a heterogeneous rock mass at the metric scale. The flaser-granitoid typically exposes a lithological anisotropy at the 10 m scale, constituted by the stacking of meta-basalt and meta-granitoid lineated units. The quarry in Heppenheim (HP) (Figure 2c,d) includes a large volume of a faulted granodiorite affected by a normal to trans-tensive fault system at the URG border. Fault cores with strong fracture intensity and clay alteration are exhibited (Figure 2c). These examples allow an investigation of the topology and dimensions of fracture properties in granodioritic rocks. In the southeastern part of the Unit III, the Tromm Granite is a medium- to coarse-grained, orthoclase-rich, biotite-bearing and often reddish granitic rock, with local amphibolite bodies preferentially present in its southern part (named Schollenagglomerat) (Ober Mengelbach (OM)). The Tromm Granite is delimited in the East by the major shearing Otzberg fault zone (Figure 1), and several outcrops are sampled along the fault damage zone, with variable distance, in Weschnitz Valley (WV), Hammelbach (HB), Streitsdöll (SD) and Borstein, Zotzenbach (ZBA). This diversity of outcrops within the Tromm provides an overview of the variability of the architectures of fracture networks within a faulted granitic pluton, with various degrees of fracture intensities and fracture directions (parallel to the main fault system, and conjugated structures (Figure 2e)).

4.3. Geometrical Features of the Fracture Network

Orientation from the LiDAR dataset was extracted from 10 locations (Figure 4). The Lichtwiese orientation dataset is extracted from the GIS interpretation as the investigated fracture planes do not have sufficient relief to be detected by the Ransac algorithm.

The main orientations identified are NNW–SSE (MZB, LD, MUL, ZBG, HOX, HB, SD, OM), NW–SE (MZB, ZBG, WV), NE–SW (MZB, SD, WV and HP), and NNE–SSW (MZB, MUL, ZBA). Fracture length distributions are extracted from the GIS interpretation (Figure 5a), and reflect the apparent length of the fractures. Mean fracture length varies from 0.54 to 16.82 m on the sampled sections, a minimum length of down to 0.01 m, and a maximum sampled length of 49.26 m overall. The fracture length distribution shows variable power-law trends depending on the lithology, with b values varying from -2.54 to -1.02.

Linear fracture density (P10) varies in the sampled locations from 0.15 to 7.74 frac·m^{-1}, with an average P10 of 2.17 frac·m^{-1}. Areal fracture density (P20) varies from 0.01 to 20.16 frac·m^{-2}, with an average P20 of 3.4 frac·m^{-2}. The low value of minimal P20 is explained by the resolution of the concerned profile in Heppenheim. Profile 5 is a long-distance profile in which few fractures are identifiable in the image. Thus, the apparent density is low. Profiles 1 to 4 in the same location were acquired closer to the quarry wall and allowed a better resolution and a higher number of identified fractures. Areal fracture intensity (P21) varies from 0.17 to 12.54 m·m^{-2}, with an average P21 of 3.15 m·m^{-2}.

Fracture spacing (C_v, unitless) varies between 0.51 and 2.4, with an average C_v of 0.97, near to 1. Fracture network connectivity (C_L,unitless) varies from 1.53 to 5.64, with an average of 3.6 and a dispersion of 0.31 (Figure 5b). The fracture connectivity is variable depending on the lithology, with granodiorites from Heppenheim and gabbros from Mühltal presenting the higher connectivities.

4.4. Semi-Artificial Discrete Fracture Network Models

The fracture network characteristics and statistics are implemented in two DFN models (Figure 6). These two cases illustrate two sub-surface configurations. Case 1, LD, refers to the dataset from Lichtwiese and is parametrised for an 800 m depth to conceptualise a medium-deep borehole heat-storage reservoir. For this model, four fracture sets are parametrised. The fracture length distribution follows a power law of 2.2, and the DFN model fits density and orientation features referenced in Table 4, case 1.

The second case is based on the Heppenheim dataset and aims to represent the fracture network of a clustered and faulted deep geothermal reservoir. Thus, the parametrised depth is 4000 m. Fracture length distribution follows a power law, and three fracture clusters are implemented, with orientation features listed in Table 4, case 2. In these two cases, different scenarios considering fracture topology (termination), the influence of the stress field on aperture, and different ratios of effective fractures are tested (Table 5), and aperture distribution and permeability tensor terms are analysed (case 1, Table 6; case 2, Table 7).

Table 6. Case 1 DFN models; aperture and permeability tensor distribution, with K_{xx}, K_{yy} and K_{zz} and permeability tensor magnitudes (K_1, K_2 and K_3), as well as main tensor orientation (KTS, strike and KTD, dip).

Model	Number	Termination (1/0)	% Open	Shear (x/o)	Aperture Mean (m)	std	log(K_{xx})	log(K_{yy})	log(K_{zz})	log(K_1)	log(K_2)	log(K_3)	KTS (N° E)	KTD (°)
LD	1	1	1	o	2.66×10^{-6}	1.33×10^{-6}	−16.32	−16.62	−16.20	−16.28	−16.38	−16.73	179	64
LD	2	1	10	o	2.92×10^{-6}	1.42×10^{-6}	−15.78	−15.81	−15.58	−15.57	−15.67	−15.98	127	34
LD	3	1	100	o	2.91×10^{-6}	1.41×10^{-6}	−14.66	−14.70	−14.47	−14.47	−14.60	−14.78	163	16
LD	4	0	10	o	2.91×10^{-6}	1.40×10^{-6}	−16.06	−15.99	−15.81	−15.03	−15.12	−15.49	128	36
LD	5	0	10	x	1.48×10^{-5}	8.56×10^{-6}	−13.29	−13.33	−13.16	−15.12	−15.23	−15.48	141	56
LD	6	0	1	o	2.92×10^{-5}	1.48×10^{-5}	−13.47	−13.66	−13.31	−13.32	−13.45	−13.73	177	63
LD	7	1	1	x	2.41×10^{-6}	1.93×10^{-6}	−16.38	−16.71	−16.28	−16.28	−16.38	−16.73	179	64
LD	8	1	100	x	1.52×10^{-5}	1.99×10^{-5}	−15.01	−15.51	−14.98	−14.97	−15.02	−15.51	179	38
LD	9	0	100	x	1.52×10^{-5}	1.99×10^{-5}	−11.89	−12.21	−11.82	−11.81	−11.90	−12.22	179	31
LD	10	1	10	x	1.48×10^{-5}	8.56×10^{-6}	−16.82	−17.02	−16.67	−16.66	−16.80	−17.05	168	30
LD	11	0	1	x	2.57×10^{-6}	1.94×10^{-6}	−16.32	−16.62	−16.20	−16.20	−16.31	−16.63	179	63
LD	12	0	100	o	2.91×10^{-6}	1.41×10^{-6}	−14.77	−14.77	−14.56	−14.56	−14.69	−14.87	110	16
LD	13	0	100	o	8.67×10^{-4}	3.22×10^{-4}	−16.84	−16.70	−16.55	−16.55	−16.63	−17.10	172	68
LD	14	0	100	x	3.10×10^{-6}	4.67×10^{-6}	−17.08	−17.61	−17.03	−17.02	−17.08	−17.63	179	72

Table 7. Case 2 DFN models aperture and permeability tensor distribution, with K_{xx}, K_{yy} and K_{zz} and permeability tensor magnitudes (K_1, K_2 and K_3), as well as main tensor orientation (KTS, strike and KTD, dip).

Model	Number	Termination (1/0)	% Open	Shear (x/o)	Aperture Mean (m)	std	log(K_{xx})	log(K_{yy})	log(K_{zz})	log(K_1)	log(K_2)	log(K_3)	KTS (N° E)	KTD (°)
HP	1	0	100	x	1.98×10^{-6}	1.39×10^{-6}	−16.19	−16.34	−16.10	−16.08	−16.19	−16.38	172	35
HP	2	0	100	o	2.66×10^{-6}	9.63E−07	−16.17	−16.08	−15.93	−15.92	−16.03	−16.26	141	25
HP	3	1	100	o	2.31×10^{-6}	1.12×10^{-6}	−16.20	−16.10	−15.95	−15.94	−16.05	−16.29	135	25
HP	4	1	100	x	1.72×10^{-6}	1.37×10^{-6}	−16.22	−16.37	−16.13	−16.11	−16.22	−16.41	171	34
HP	5	0	10	x	1.60×10^{-6}	1.61×10^{-6}	−17.28	−17.26	−17.09	−17.07	−17.18	−17.42	167	51
HP	6	0	10	o	2.66×10^{-6}	9.71×10^{-7}	−17.07	−17.04	−16.87	−16.85	−16.96	−17.22	166	47
HP	7	1	10	x	1.51×10^{-6}	1.63×10^{-6}	−17.80	−18.04	−17.82	−17.08	−17.18	−17.42	168	51
HP	8	1	10	o	2.48×10^{-6}	1.06×10^{-6}	−17.09	−17.05	−16.89	−16.87	−16.98	−17.24	166	47
HP	9	0	1	o	2.65×10^{-6}	9.45×10^{-7}	−15.77	−15.84	−15.57	−16.17	−16.32	−16.57	178	70
HP	10	1	1	o	2.49×10^{-5}	1.02×10^{-5}	−14.65	−14.64	−14.41	−14.40	−14.54	−14.80	178	70
HP	11	0	1	x	1.04×10^{-5}	3.94×10^{-6}	−17.64	−17.62	−17.39	−15.56	−15.71	−15.96	178	70
HP	12	1	1	x	1.79×10^{-6}	1.40×10^{-6}	−17.59	−17.82	−17.47	−17.46	−17.59	−17.86	178	71
HP	13	0	100	o	3.12×10^{-6}	1.17×10^{-6}	−17.60	−17.08	−17.00	−16.99	−17.05	−17.75	174	77
HP	14	0	100	x	3.75×10^{-7}	2.16×10^{-6}	−17.62	−18.01	−17.51	−17.51	−17.60	−18.06	179	82

4.4.1. Aperture Distributions

Two methodologies were considered to estimate fracture aperture. They show a slightly variable mean aperture and exhibit a difference of heterogeneity in the fracture aperture distribution within the 3D models (Figure 7; Tables 6 and 7). Aperture distributions, in case (1) (LD, Table 6), considering aperture as a function of fracture length, vary between 7.7×10^{-8} m and 2.46×10^{-3} m, with an average aperture of 1.30×10^{-4} m. In the same case (1) model, shear-dependent apertures vary between zero and 7.7×10^{-8} m and 5.15×10^{-4} m, with an average aperture of 9.73×10^{-6} m. Apertures determined by shear dependency are more than one magnitude smaller than apertures that are length-dependent. For case (2) (HP; Table 7), aperture as a function of fracture length shows a minimum value of 0, i.e., closed fractures, a maximum of 1.95×10^{-4} m and an average of 5.83×10^{-6} m. When parametrised as a shear dependent, aperture varies between 0 and 8.33×10^{-5} m, with a mean aperture of 2.77×10^{-6} m. For shear dependent apertures, fractures favourably oriented within the stress field exhibit two to three times larger apertures (Figure 7b,d) than in the case where apertures are a function of fracture radius (Figure 7a,c), but only for a small numbers of fractures.

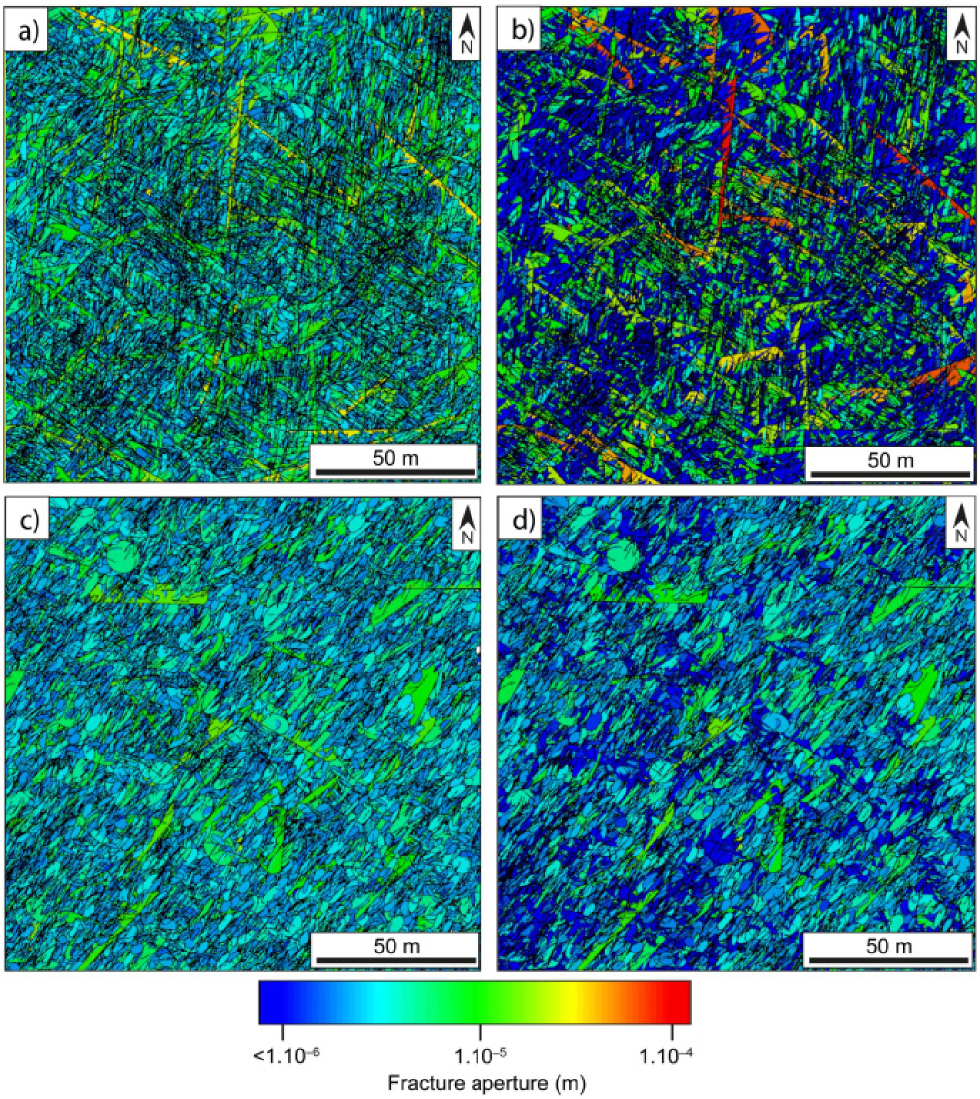

Figure 7. Fracture aperture maps for (**a**) DFN case 1, 10% of open fractures, andfracture length dependant aperture and (**b**) DFN case 1, 10% of open fractures, and shear dependent aperture, and (**c**) DFN case 2, 10% of open fractures, andfracture length dependant aperture and (**d**) DFN case 2, 10% of open fractures, and shear dependent aperture.

4.4.2. Permeability Field

The permeability tensor is calculated after ODA [97] and results summarised for case (1) in Table 6 and for case (2) in Table 7. For case (1) (Figure 8a,b), from the 12 models issued, the average K_{xx} is $10^{-14.9}$ m^2, with lower values for the deterministic models ($10^{-16.9}$ m^2). K_{yy} average is $10^{-15.1}$ m^2, and $10^{-17.1}$ m^2 for the deterministic models. K_{zz} average is $10^{-14.7}$ m^2, with lower values for the deterministic models ($10^{-16.7}$ m^2). Tensor terms in the 12 models of case 2 (Figure 8c,d) show lower values, with an average K_{xx} of $10^{-16.7}$ m^2, K_{yy} of $10^{-16.8}$ m^2 and K_{zz} of $10^{-16.5}$ m^2. Deterministic models for case 2 also show low values of K_{xx} ($10^{-17.6}$ m^2), K_{yy} ($10^{-17.5}$ m^2) and K_{zz} ($10^{-17.2}$ m^2). The heterogeneity induced by the distribution of fracture aperture is also overprinted on the permeability field, with a more substantial anisotropy for shearing dependent permeability grids (Figure 8b,d). Maximum magnitudes of the permeability tensor (K_1,K_2,K_3) shows a similar trend. The orientation of the permeability tensor is similar for the models in which the stress field is integrated. The permeability tensor orientation variability observed for models that do not integrate the stress field suggests that the maximum permeability is oriented along the direction in which most of the fractures are present.

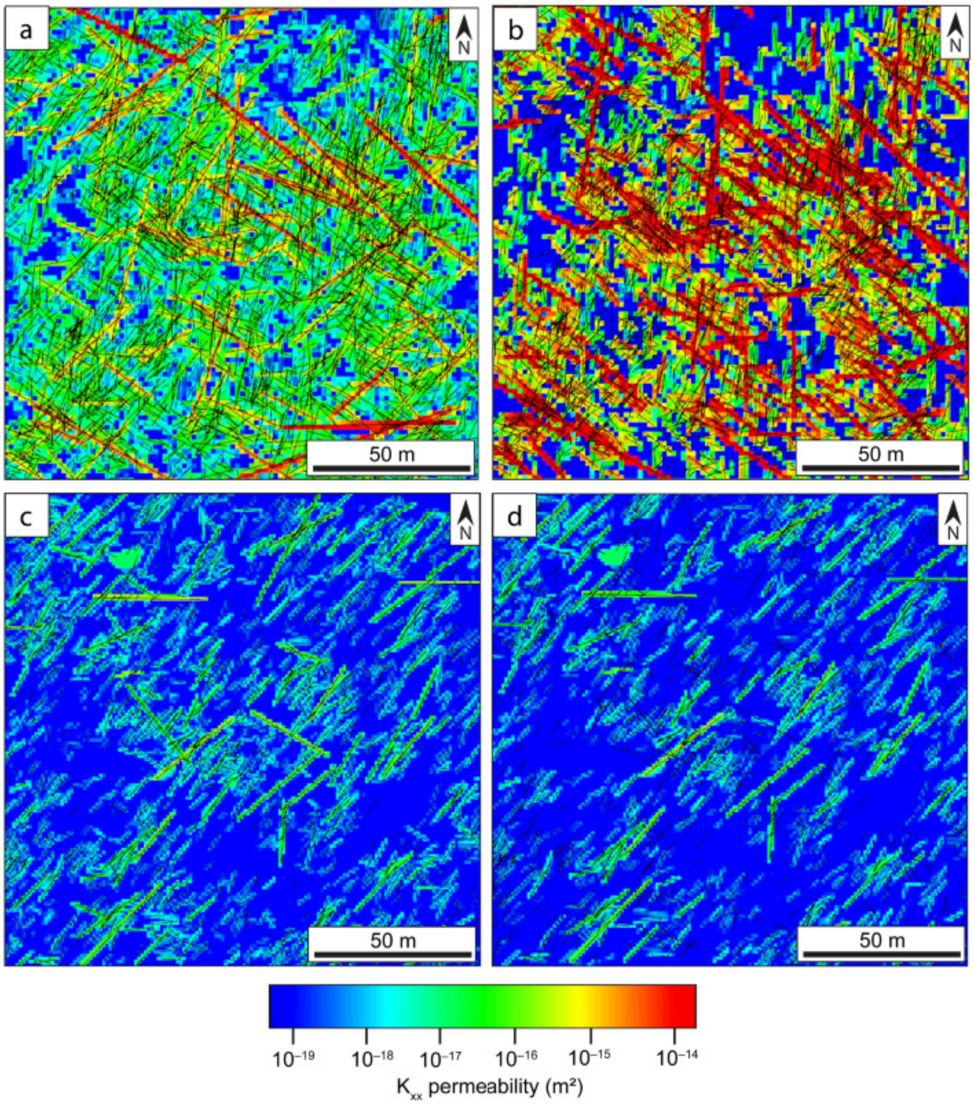

Figure 8. Equivalent permeability grid for (**a**) DFN case 1, 10% of open fractures, andfracture length dependant aperture and (**b**) DFN case 1, 10% of open fractures, and shear dependent aperture, and (**c**) DFN case 2, 10% of open fractures, andfracture length dependant aperture and (**d**) DFN case 2, 10% of open fractures, and shear dependent aperture.

5. Discussion

5.1. Near-Surface Architecture of Crystalline Reservoirs

5.1.1. Fracture Network Topology and Clustering

The fracture network topology is a key parameter in assessing the flow behaviour in crystalline rocks (Figure 5b). The fracture network exhibits Y-I nodes preferably within shearing fault zones, whereas background fracturing and normal fault deformations tend more toward an X node dominated network. Such an outcome is implemented in the choice of termination scenarios in DFN models. Models with an active fracture termination represent the Y-node prone network, and the X-node prone is represented by a non terminated network. Clustering of the fracture network is an essential component of the quantitative fracture network analysis. The clustering indeed increases the heterogeneity and the anisotropy of transfer properties with crystalline fractured reservoirs. This heterogeneity, occurring at different scales, and in fault zones and in background fracture network, needs to be characterised quantitatively to increase the accuracy of reservoir models and potential assessments. The diversity of fault zone configuration investigated in this study also reflects various ranges of fracture network clustering, which can be assessed by the variability of relative spacing profiles in distance occurrence frequencies diagrams (Figure 9). With such representations, the potential clustering of the fracture distribution can be detected [15,101]. The black line represents a random distribution, and the higher the deviation from this curve, the stronger the clustering. In granitic and granodioritic outcrops, the clustering is marked by the presence of strong deviations from the normal distribution, by Cv values greater than 1, and by a Y node connected network. In the core of outcropping fault zones, as in Heppenheim (Figure 9e,f), the fracture is marked by a mixed X and Y topology, indicating a discretisation and a preferential localisation of the deformation volumes around these corridors. At a further distance from the fault core (Streitsdölle, Tromm granite), the background fracture network is also showing a Y node-prone topology. However, the clustering is also relatively intense, as translated by the numerous slope break points (Figure 9g,h). In the Lichtwiese pit, the top view also exhibits a well-connected Y node dominated fracture network, in which the clustering is slightly less intense (Figure 9a,b). In this particular case of background fracture network at the top of the weathering zone, some fractures may be harder to identify, as the hardness of the granodiorite is weakened by weathering. In the more mafic lithologies sampled, e.g., in Mühltal (Figure 9c,d) and Obermengelbach (OM) (Figure 9i,j), the fracture network also exhibits good connectivity, with X nodes predominant outside of the faulted zones for the gabbro in Mühltal. A few profiles, orthogonal to the fault zone, show a tendency to clusterisation, underlining the localisation of deformation in such structures. The amphibolite-rich rock volume characterised in Obermengelbach is affected by a Y node dominated fracture network, in which fracture spacing has a random distribution, also marked by the smaller size of fracture segments, compared to the rest of the lithologies. This fracture network affecting the amphibolite might result from volume deformation linked to the intrusion of granitic and felsic bodies in southern crystalline Odenwald [102].

5.1.2. Multi-Scale Behaviour from Regional Scale to Outcrop Scale

The 11 sampled localities allow depiction of a multi-scale behaviour of the fracture network depending on lithology and structural context. The typology of the fracture network is linked to the lithology. Several regional shearing and faulting directions were identified on the regional lineament survey and are identical to the typical Hercynian deformation directions reported [13,45,74,103]. The major shearing and crustal boundaries of the NURG basement increase the expression of NE–SW lineaments. NNE–SSW striking lineaments on the western side of the Odenwald are associated mainly with the Cenozoic rift activity [44,45,103].

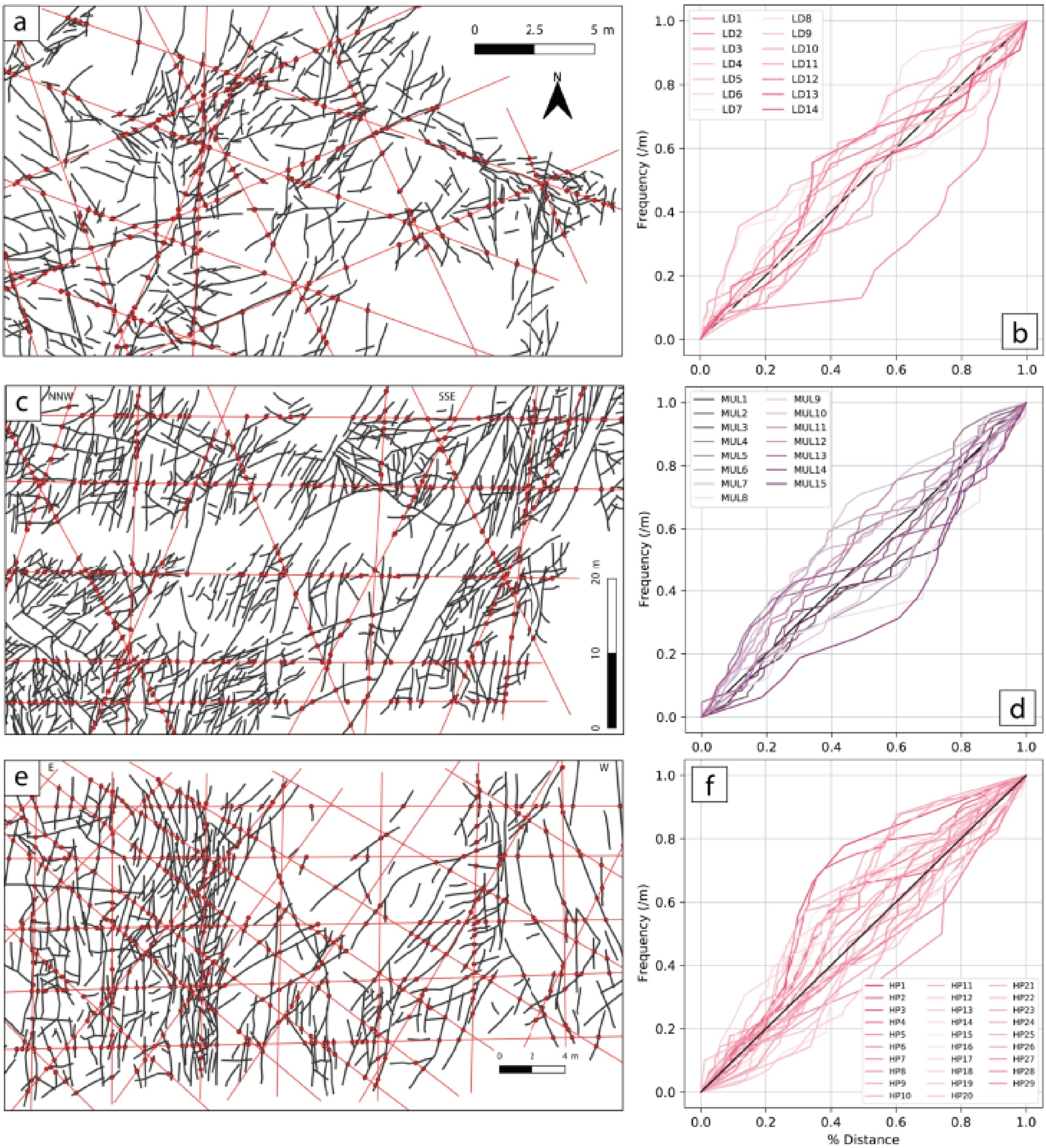

Figure 9. *Cont*.

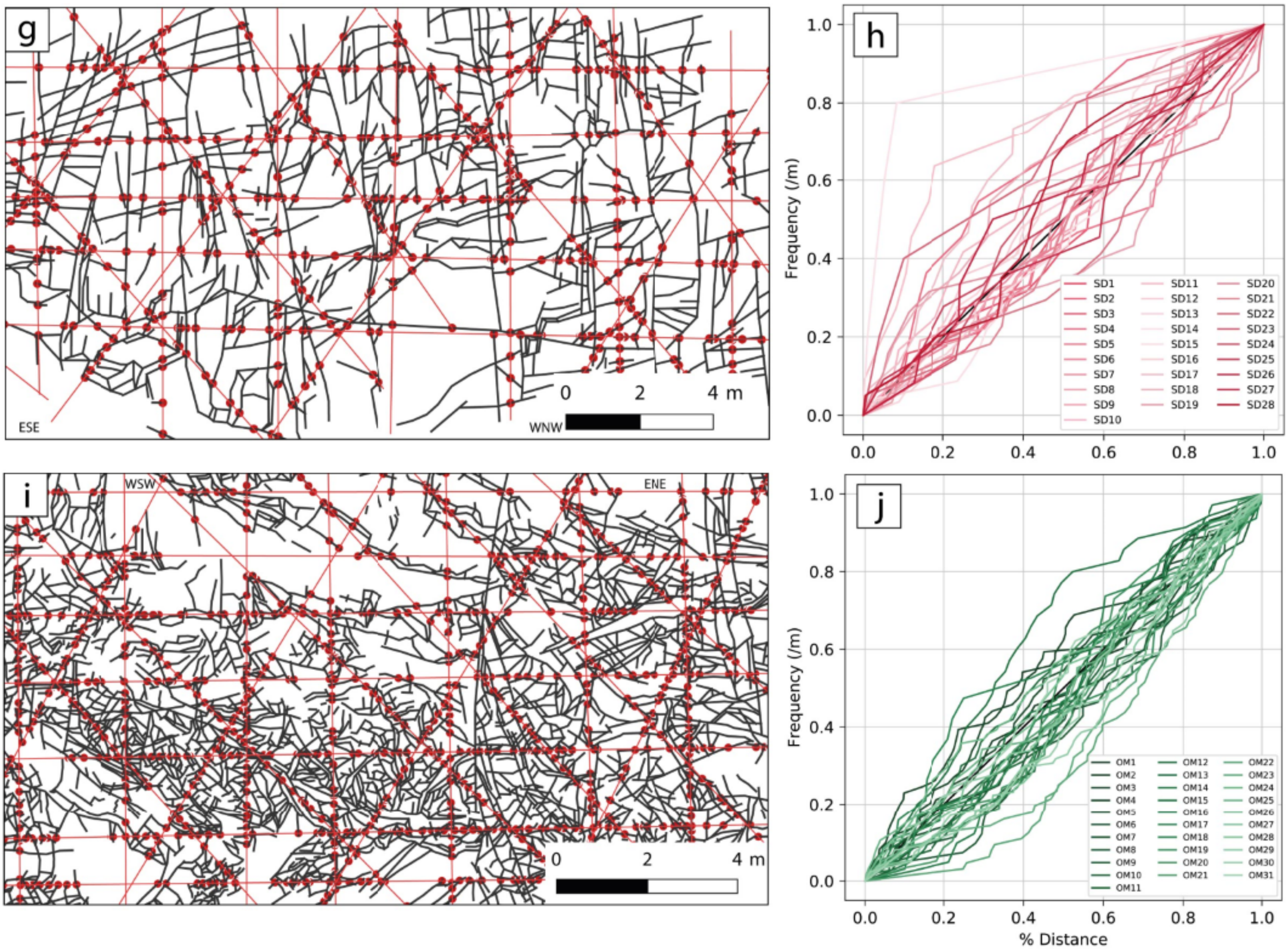

Figure 9. Clustering of the fracture network in the Odenwald. (**a**) Fracture map from the granodioritic Lichtwiese (LD) damage zone, (**b**) Distance-occurrence frequency diagram associated with mapping. (**a**,**c**) Fracture 2D profile in a faulted gabbro (Mühltal (MUL)). (**d**) Distance–occurrence frequency diagram associated with mapping, (**c**,**e**) Fracture 2D profile in a faulted granodioritic Weschnitz pluton, in Heppenheim quarry (HP), (**f**) Distance–occurrence frequency diagram associated with mapping, (**e**,**g**) Fracture 2D profile in the granitic Tromm pluton (Streitsdölle (SD)), (**h**) Distance–occurrence frequency diagram associated with mapping, (**g**,**i**) Fracture 2D profile in an amphibolite outcrop in Obermengelbach (OM), (**j**) Distance–occurrence frequency diagram associated with mapping (**i**). For maps and profiles (**a**,**c**,**e**,**g**,**i**), black lines represent the digitised fractures, and red lines and dots the artificial scanlines used to compute clustering features. The applied colour code in the distance–occurrence frequency diagrams in (**b**,**d**,**f**,**h**,**j**) is related to the sampled lithology (see Figure 1).

The normalised cumulative length distribution (Figure 10) exhibits a multi-scale power-law behaviour, with a slope value of −2.02 similar to previous investigations, in crystalline rocks outcropping on the URG shoulders (Vosges, −2.05 [13], Schwarzwald between −2.0 and −2.5 [103], Odenwald −2.03 [15]).

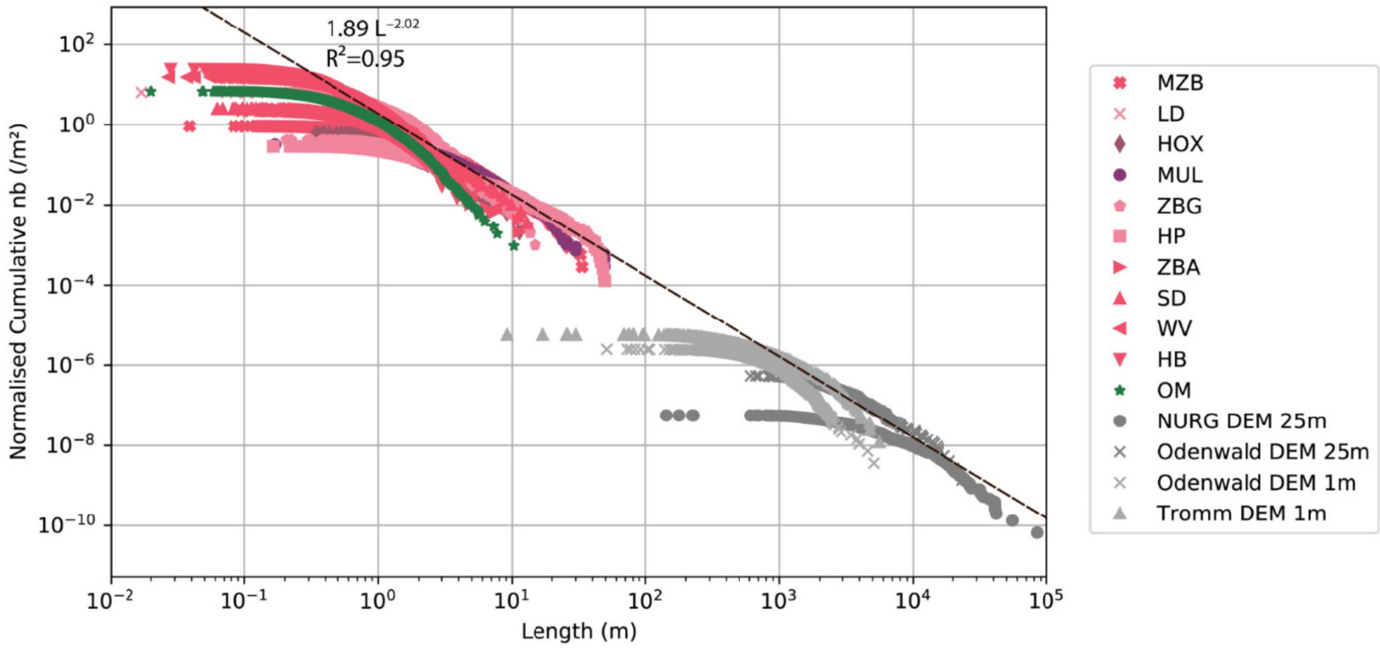

Figure 10. Cumulative length distribution and orientation roses for the Odenwald, compared with trends reported in the Schwarzwald and the Vosges (Bertrand et al., 2018; Meixner et al., 2016, 2018).

The hydraulic behaviour of each of these structures depends on the stress field. The dilation-slip tendency [63] suggests that shear reactivation in the strike-slip regime affects mainly NNE–SSW and ENE–WSW systems, thus indicating a preferential fluid flow, along with structures with a similar orientation within the current stress field.

5.2. Estimation of Flow Properties in Deep-Seated Reservoirs

The permeability field was assessed from the DFN models with an ODA approach and considers variable aperture distribution controlled by fracture size or shear dependency, e.g., influence of the stress field. Datasets from the Soultz-sous-Forêts site present mean permeabilities for the granitic basement ranging from 1.10^{-17} to 11.10^{-15} m^2 [104,105]. When compared to these pre-existing permeability fields in crystalline rocks, several of these values are out of range, suggesting that several of the scenarios exhibiting 100% of active fractures are not realistic. Stochastic models for case 1 considering 1% and 10% active fractures present permeabilities between $10^{-16.8}$ and $10^{-13.1}$ m^2, and aperture distributions between 2.10^{-7} and 3.10^{-3} m. Permeabilities estimated in previous models refer to the range between 1.10^{-17} to 1.10^{-15} m^2 [104,105] compared with deep reservoirs. In case 1, the heat storage site is situated only at 800 m. Thus the high permeabilities between 1.10^{-15} and 1.10^{-13} in fractured areas are likely to be encountered. For case 2, permeability values range between 10^{-18} and $10^{-14.5}$ m^2, also coherent with the observations in Soultz-sous-Forêts granite on the lower and upper boundary. These values are also coherent with the range estimated in previous studies for deep-seated crystalline reservoirs [24,104,106,107].

The DFN and ODA calculations illustrate critical parameters of aperture estimation (Figures 7 and 8). The fracture aperture distribution shows here a clear impact on permeability. Calculated permeability field average values show the influence of shearing and depth on fracture aperture, thus on the anisotropy of the permeability field for shearing dependent permeability grids (Figure 8). Heterogeneity of the permeability tensor on xy- and yz-planes is increased in DFN models, which include the shear correlated aperture distribution (Figure 11). When comparing in a cross-plot the relationship between K_{xy} and K_{yz} (Figure 11), shear dependent permeability estimations induce a larger lateral and vertical heterogeneity, with points situated on the top right or bottom left part of the cross-plot. On the contrary, permeability ranges issued from the length dependent aperture are situated in the central part of the graph. This exhibits a more homogeneous permeability tensor for apertures directly extracted from fracture length. The modelling of aperture distribution in further steps should include subsurface well datasets and transmissivity quantification to upscale reservoir transfer properties. For this first-order estimation, the Mohr-Coulomb criteria are considered here. Shear dependency and additional methods to approach this [32,33,36,108–110], and the deciphering of fracture aperture behaviour at the sub-seismic scale, should be extensively considered in further studies. Additional investigation of the fracture aperture and characterisation of the hydraulically active fracture network can be implemented for borehole investigations.

5.3. Structural Uncertainties Related to Sub-Surface Transfer

Transferring analogue datasets to subsurface conditions requires several strong hypotheses, which could be addressed both by stochastic or deterministic approaches to permeability estimation [111,112]. This study examined stress field and shear influence on fracture aperture at different depths, following the primary hypothesis that stress field depends on depth, without considering additional fluid pressure or local overpressure and/or dilation. In the frame of an upscaling to reservoir conditions for a real case study, only borehole datasets with in-situ stress fields can help to validate such a hypothesis. though, even with borehole data, uncertainties remain.

The type 1 uncertainty can be reduced by acquiring and implementing borehole data. This type of uncertainty can include orientation spacing and distribution of fractures that are recovered from the fracture logging. Additionally, borehole data are the only way to deterministically assess aperture distribution. Indeed, this aperture distribution is not representative at surface conditions, as it is enhanced by weathering and outcropping. Fracture network properties change with depth, as demonstrated by the comparison with the datasets for Soultz wells [104,105].

Not only the nature of the fractures themselves are subject to uncertainty; as subsurface conditions are different, there is an inherent heterogeneity on a larger scale as both lateral conditions change. Thus, intrinsic properties can differ from their surface analogue counterparts. This means that, even if borehole data is present to calibrate DFN models, uncertainties increase along with distance to the borehole. Next to borehole data, high density 3D seismic data can indicate porosity, including secondary porosity induced by fractures [113], reducing some of the type 1 and type 2 errors.

Outcrops are useful to reduce uncertainty about heterogeneity under the hypothesis of the similarity of the fracture network organisation (clustering, fracture spacing, topology). They also indicate fracture orientations and dimensions and their variability. While these uncertainties are present, outcrop analogue investigations remain a reliable method to estimate fracture network features in the subsurface.

5.4. Applicability of the Conceptual Model of Crystalline Faulted Rocks

With increasing depth, for large size fractures aperture range is affected by the vertical stresses and can modify the orientation of the permeability anisotropy in fractured zones. Thus, this emphasises the need for discrete subsurface datasets, from well logs and cores, to acquire calibration data for fracture models in order to achieve a proper permeability field assessment in subsurface conditions. The stochastic approach used here provides a first-order estimation of the permeability field in the sub-surface, which is helpful in decreasing the uncertainties related to the hydraulic behaviour of the rock mass. Still, such an explorative DFN model approach can not replace exploration wells and in-situ measurement of hydraulic properties.

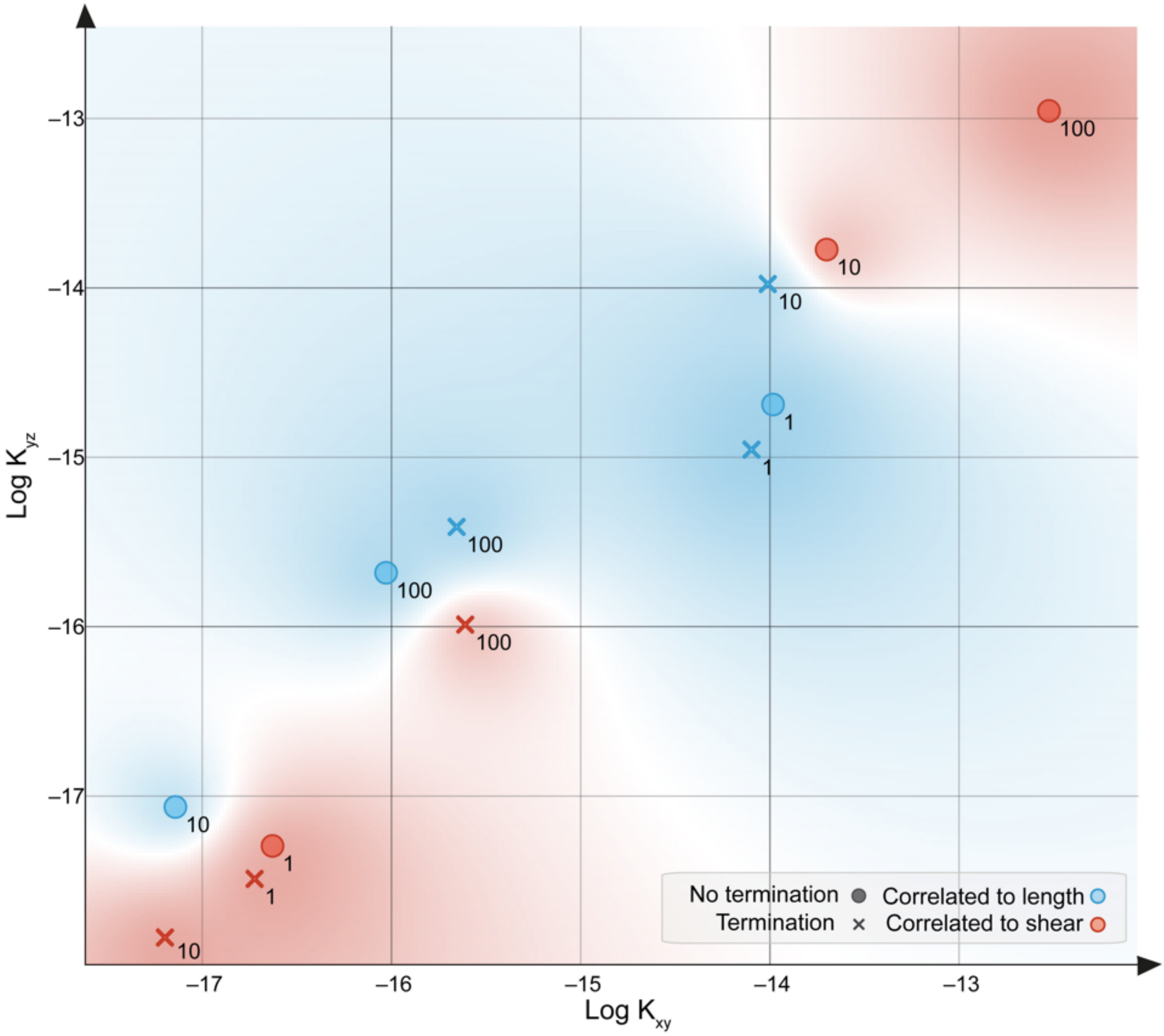

Figure 11. K_{xy} versus K_{yz} cross plot showing heterogeneities of permeability tensor term implied by the shear dependency of fracture aperture and fracture termination parametrisation, values from case 1 (LD).

A strong emphasis should be placed on thermo- and poro-elastic stress fields, as they impact transfer properties in such rock types. Fracture network geometry and porosity are critical factors in modelling fluid transfer, thus affecting the technical potential of geothermal exploitation or heat storage at a specific depth interval in the subsurface. This conceptual model approach needs also to include fluid behaviour and critical fluid pressure stresses involved in the aperture distribution in the subsurface [105,114]. No matter which application is planned in the subsurface, the effect of the stress field has to be considered, i.e., target closed fracture intervals for heat storage, to avoid any heat loss due to fluid flow. On the other side of the spectrum, targeted intervals are where fractures may be reactivated for productive geothermal intervals, and a favourable stress field maintains this aperture effective.

The realistic permeability range obtained here suggests that only a fraction of the observed fracture network displays effective flow behaviour. Permeability tensor anisotropy, showing up to one order of magnitude difference, should also be considered in geo-energy projects. In the case of a geothermal plant, the geothermal doublets trajectory should be designed accordingly. Adapted well designs should emphasise open-hole sections orthogonal to fracture orientation with a favourable effective aperture. Such favourable fractures are mainly orthogonal to the principal deviatoric strain in models that integrate the stress field. Such features indeed exhibit the most promising permeabilities. In contrast, if heat storage is targeted, these highly permeable fractures are to be avoided, as such structural features could lead to a leak of heat through the migration of the thermal plume through such structures. Such process would lead to a decrease in storage efficiency.

Secondly, the flow behaviour in such fractured crystalline reservoirs is also linked to overpressure and stress releases. These processes can contribute to seismicity, both near-well and far-field. Induced seismicity, particularly in well enhancement and well stimulation, aims to improve the permeability of the rock mass. Structures with a dense and connected 3D network have to be targeted rather than localised and highly clusterised structures to avoid large seismic events and ensure a favourable permeability. Fracture network characterisation and modelling also help to interpret and localise the seismic response of the reservoir under perturbed stress conditions [1,115]. Stress magnitudes and their relationship with the fracture network, its potential reactivation, as single seismic event or as creep mechanisms [116], and its hydraulic behaviour also have to be assessed to ensure efficient geothermal reservoir management [117].

6. Conclusions

Characterising crystalline rocks within various structural contexts and fracture network configurations is essential for semi-artificial DFN workflow. As the crystalline basement is not homogeneous in terms of lithology and structural framework, the aim is to provide a variety of fracture network datasets and property distributions, from the length, orientation, and topology. These datasets increase the quantified knowledge of the structural architecture of such rock materials at a sub-seismic scale. Their analysis reflects the particularities linked to lithological and local structural contexts. The topology of the fracture network is dependent on the lithology and the structural context. The regional lineament analysis, combined with the local outcrop analogue study, underline the multi-scale character of the crystalline fault and fracture network. The normalised cumulative length distribution exhibits a power-law behaviour over seven ranges of magnitude, with a slope value of −2.02, similar to previous investigations, in crystalline rocks outcropping on the URG shoulders. Two case studies for heat-storage and deep-geothermal reservoirs were implemented following three-dimensional and geometrical fracture network insights from surface analogues and applying different scenarios to assess fracture aperture. The fracture aperture distribution strongly affects the permeability field in the approach used here. The stress field dependency of the fracture hydraulic behaviour is critical compared to the lithology, as the fracture network controls the flow in such crystalline rocks. In comparison with pre-existing subsurface data, it is essential to implement the stress field dependency to assess a proper hydraulic model of the fracture network, including the permeability anisotropy implied by the fracture network. Thus, this study gives valuable insights into integrating outcrops' analogue data in the pre-feasibility approach to industrial applications.

Author Contributions: Conceptualisation, C.B., L.S., I.S.; methodology, C.B., L.S., I.S.; validation, C.B., I.S.; investigation, C.B., M.F., L.S.; uncertainty quantification, J.v.d.V.; writing—original draft preparation, C.B., L.S.; writing—review and editing, L.S., M.F., I.S., J.v.d.V.; project administration, I.S.; funding acquisition, I.S. All authors have read and agreed to the published version of the manuscript.

Funding: This research was supported by the Interreg NWE Programme through the Roll-out of Deep Geothermal Energy in North-West Europe (DGE-ROLLOUT) Project (www.nweurope.eu/DGE-ROLLOUT accessed on 1 December 2021). The Interreg NWE Programme is part of the European Cohesion Policy and is financed by the European Regional Development Funds (ERDF). We acknowledge the support of the APC by the Deutsche Forschungsgemeinschaft (DFG—German Research Foundation) and the Open Access Publishing Fund of the Technical University of Darmstadt.

Institutional Review Board Statement: Not applicable.

Informed Consent Statement: Not applicable.

Data Availability Statement: The following are available online at the following repository: https://doi.org/10.48328/tudatalib-774 accessed on 1 December 2021.

Acknowledgments: We would like to thank the HLNUG who provided digital elevation data, Sebastian Schröder and the municipalities of Wald-Michelbach and Rimbach for giving us access to the quarries in the Tromm Granite. We also would like to thank the Mitteldeutsche Hartstein-Industrie AG for granting access to the Mainzer Berg and Mühltal quarry. RÖHRIGgranit GmbH is thanked for granting us access to their quarries in Heppenheim.

Conflicts of Interest: The authors declare no conflict of interest.

References

1. Baujard, C.; Genter, A.; Dalmais, E.; Maurer, V.; Hehn, R.; Rosillette, R.; Vidal, J.; Schmittbuhl, J. Hydrothermal Characterization of Wells GRT-1 and GRT-2 in Rittershoffen, France: Implications on the Understanding of Natural Flow Systems in the Rhine Graben. *Geothermics* **2017**, *65*, 255–268. [CrossRef]
2. Bertrand, L.; Géraud, Y.; Diraison, M. Petrophysical Properties in Faulted Basement Rocks: Insights from Outcropping Analogues on the West European Rift Shoulders. *Geothermics* **2021**, *95*, 102144. [CrossRef]
3. Frey, M.; Weinert, S.; Bär, K.; van der Vaart, J.; Dezayes, C.; Calcagno, P.; Sass, I. Integrated 3D Geological Modelling of the Northern Upper Rhine Graben by Joint Inversion of Gravimetry and Magnetic Data. *Tectonophysics* **2021**, *813*, 228927. [CrossRef]
4. Freymark, J.; Sippel, J.; Scheck-Wenderoth, M.; Bär, K.; Stiller, M.; Kracht, M.; Fritsche, J.-G. Heterogeneous Crystalline Crust Controls the Shallow Thermal Field—A Case Study of Hessen (Germany). *Energy Procedia* **2015**, *76*, 331–340. [CrossRef]
5. Freymark, J.; Sippel, J.; Scheck-Wenderoth, M.; Bär, K.; Stiller, M.; Fritsche, J.-G.; Kracht, M. The Deep Thermal Field of the Upper Rhine Graben. *Tectonophysics* **2017**, *694*, 114–129. [CrossRef]
6. Baillieux, P.; Schill, E.; Edel, J.-B.; Mauri, G. Localization of Temperature Anomalies in the Upper Rhine Graben: Insights from Geophysics and Neotectonic Activity. *Int. Geol. Rev.* **2013**, *55*, 1744–1762. [CrossRef]
7. Baillieux, P.; Schill, E.; Abdelfettah, Y.; Dezayes, C. Possible Natural Fluid Pathways from Gravity Pseudo-Tomography in the Geothermal Fields of Northern Alsace (Upper Rhine Graben). *Geotherm. Energy* **2014**, *2*, 16. [CrossRef]
8. Bossennec, C.; Géraud, Y.; Moretti, I.; Mattioni, L.; Stemmelen, D. Pore Network Properties of Sandstones in a Fault Damage Zone. *J. Struct. Geol.* **2018**, *110*, 24–44. [CrossRef]
9. Glaas, C.; Vidal, J.; Genter, A. Structural Characterization of Naturally Fractured Geothermal Reservoirs in the Central Upper Rhine Graben. *J. Struct. Geol.* **2021**, *148*, 104370. [CrossRef]
10. Vidal, J.; Genter, A. Overview of Naturally Permeable Fractured Reservoirs in the Central and Southern Upper Rhine Graben: Insights from Geothermal Wells. *Geothermics* **2018**, *74*, 57–73. [CrossRef]
11. Walter, B.F.; Burisch, M.; Fusswinkel, T.; Marks, M.A.W.; Steele-MacInnis, M.; Wälle, M.; Apukhtina, O.B.; Markl, G. Multi-Reservoir Fluid Mixing Processes in Rift-Related Hydrothermal Veins, Schwarzwald, SW-Germany. *J. Geochem. Explor.* **2018**, *186*, 158–186. [CrossRef]
12. Bertrand, L.; Géraud, Y.; Le Garzic, E.; Place, J.; Diraison, M.; Walter, B.; Haffen, S. A Multiscale Analysis of a Fracture Pattern in Granite: A Case Study of the Tamariu Granite, Catalunya, Spain. *J. Struct. Geol.* **2015**, *78*, 52–66. [CrossRef]
13. Bertrand, L.; Jusseaume, J.; Géraud, Y.; Diraison, M.; Damy, P.-C.; Navelot, V.; Haffen, S. Structural Heritage, Reactivation and Distribution of Fault and Fracture Network in a Rifting Context: Case Study of the Western Shoulder of the Upper Rhine Graben. *J. Struct. Geol.* **2018**, *108*, 243–255. [CrossRef]
14. Place, J.; Géraud, Y.; Diraison, M.; Herquel, G.; Edel, J.-B.; Bano, M.; Le Garzic, E.; Walter, B. Structural Control of Weathering Processes within Exhumed Granitoids: Compartmentalisation of Geophysical Properties by Faults and Fractures. *J. Struct. Geol.* **2016**, *84*, 102–119. [CrossRef]
15. Bossennec, C.; Frey, M.; Seib, L.; Bär, K.; Sass, I. Multiscale Characterisation of Fracture Patterns of a Crystalline Reservoir Analogue. *Geosciences* **2021**, *11*, 371. [CrossRef]
16. Ceccato, A.; Viola, G.; Antonellini, M.; Tartaglia, G.; Ryan, E.J. Constraints upon Fault Zone Properties by Combined Structural Analysis of Virtual Outcrop Models and Discrete Fracture Network Modelling. *J. Struct. Geol.* **2021**, *152*, 104444. [CrossRef]
17. Weinert, S.; Bär, K.; Sass, I. Database of Petrophysical Properties of the Mid-German Crystalline Rise. *Earth Syst. Sci. Data* **2021**, *13*, 1441–1459. [CrossRef]
18. Bär, K.; Reinsch, T.; Bott, J. The PetroPhysical Property Database (P^3)—A Global Compilation of Lab-Measured Rock Properties. *Earth Syst. Sci. Data* **2020**, *12*, 2485–2515. [CrossRef]
19. Edel, J.-B.; Schulmann, K. Geophysical Constraints and Model of the "Saxothuringian and Rhenohercynian Subductions—Magmatic Arc System" in NE France and SW Germany. *Bull. Soc. Géol. Fr.* **2009**, *180*, 545–558. [CrossRef]
20. Edel, J.-B.; Schulmann, K.; Rotstein, Y. The Variscan Tectonic Inheritance of the Upper Rhine Graben: Evidence of Reactivations in the Lias, Late Eocene–Oligocene up to the Recent. *Int. J. Earth Sci. (Geol. Rundsch.)* **2007**, *96*, 305–325. [CrossRef]

21. McCaffrey, K.J.W.; Holdsworth, R.E.; Pless, J.; Franklin, B.S.G.; Hardman, K. Basement Reservoir Plumbing: Fracture Aperture, Length and Topology Analysis of the Lewisian Complex, NW Scotland. *J. Geol. Soc.* **2020**, *177*, 1281–1293. [CrossRef]
22. Trice, R. Basement Exploration, West of Shetlands: Progress in Opening a New Play on the UKCS. *Geol. Soc. Lond. Spec. Publ.* **2014**, *397*, 81–105. [CrossRef]
23. Bonter, D.A.; Trice, R. An Integrated Approach for Fractured Basement Characterization: The Lancaster Field, a Case Study in the UK. *Pet. Geosci.* **2019**, *25*, 400–414. [CrossRef]
24. Frey, M.; Bossennec, C.; Seib, L.; Bär, K.; Sass, I. Interdisciplinary Fracture Network Characterization in the Crystalline Basement: A Case Study from the Southern Odenwald, SW Germany. *Solid Earth Discuss.* **2021**, 1–35. [CrossRef]
25. Li, X.; Li, D.; Xu, Y.; Feng, X. A DFN Based 3D Numerical Approach for Modeling Coupled Groundwater Flow and Solute Transport in Fractured Rock Mass. *Int. J. Heat Mass Transf.* **2020**, *149*, 119179. [CrossRef]
26. Lei, Q.; Latham, J.-P.; Tsang, C.-F. The Use of Discrete Fracture Networks for Modelling Coupled Geomechanical and Hydrological Behaviour of Fractured Rocks. *Comput. Geotech.* **2017**, *85*, 151–176. [CrossRef]
27. Le Goc, R.; Darcel, C.; Davy, P. Advanced DFN Models from Multi-Support Data for Underground Facilities. *Procedia Eng.* **2017**, *191*, 1015–1022. [CrossRef]
28. Bardossy, G.; Fodor, J. Evaluation of Uncertainties and Risks. In *Geology: New Mathematical Approaches for Their Handling*; Springer Science & Business Media: Berlin/Heidelberg, Germany, 2004; ISBN 978-3-540-20622-4.
29. Mann, C.J. Uncertainty in Geology. In *Computers in Geology—25 Years of Progress*; Oxford University Press, Inc.: New York, NY, USA, 1993; pp. 241–254. ISBN 978-0-19-508593-8.
30. Wilson, C.E.; Aydin, A.; Karimi-Fard, M.; Durlofsky, L.J.; Amir, S.; Brodsky, E.E.; Kreylos, O.; Kellogg, L.H. From Outcrop to Flow Simulation: Constructing Discrete Fracture Models from a LIDAR Survey. *AAPG Bull.* **2011**, *95*, 1883–1905. [CrossRef]
31. Voeckler, H.; Allen, D.M. Estimating Regional-Scale Fractured Bedrock Hydraulic Conductivity Using Discrete Fracture Network (DFN) Modeling. *Hydrogeol. J.* **2012**, *20*, 1081–1100. [CrossRef]
32. Bisdom, K.; Nick, H.M.; Bertotti, G. An Integrated Workflow for Stress and Flow Modelling Using Outcrop-Derived Discrete Fracture Networks. *Comput. Geosci.* **2017**, *103*, 21–35. [CrossRef]
33. Bisdom, K.; Gauthier, B.D.M.; Bertotti, G.; Hardebol, N.J. Calibrating Discrete Fracture-Network Models with a Carbonate Three-Dimensional Outcrop Fracture Network: Implications for Naturally Fractured Reservoir Modeling. *Bulletin* **2014**, *98*, 1351–1376. [CrossRef]
34. Min, K.-B.; Rutqvist, J.; Tsang, C.-F.; Jing, L. Stress-Dependent Permeability of Fractured Rock Masses: A Numerical Study. *Int. J. Rock Mech. Min. Sci.* **2004**, *41*, 1191–1210. [CrossRef]
35. French, M.E.; Chester, F.M.; Chester, J.S.; Wilson, J.E. Stress-Dependent Transport Properties of Fractured Arkosic Sandstone. *Geofluids* **2016**, *16*, 533–551. [CrossRef]
36. Lepillier, B.; Bruna, P.-O.; Bruhn, D.; Bastesen, E.; Daniilidis, A.; Garcia, Ó.; Torabi, A.; Wheeler, W. From Outcrop Scanlines to Discrete Fracture Networks, an Integrative Workflow. *J. Struct. Geol.* **2020**, *133*, 103992. [CrossRef]
37. Welsch, B.; Rühaak, W.; Schulte, D.O.; Bär, K.; Sass, I. Characteristics of Medium Deep Borehole Thermal Energy Storage. *Int. J. Energy Res.* **2016**, *40*, 1855–1868. [CrossRef]
38. Schulte, D.O.; Welsch, B.; Boockmeyer, A.; Rühaak, W.; Bär, K.; Bauer, S.; Sass, I. Modeling Insulated Borehole Heat Exchangers. *Environ. Earth Sci.* **2016**, *75*, 910. [CrossRef]
39. Formhals, J.; Hemmatabady, H.; Welsch, B.; Schulte, D.; Sass, I. A Modelica Toolbox for the Simulation of Borehole Thermal Energy Storage Systems. *Energies* **2020**, *13*, 2327. [CrossRef]
40. Dèzes, P.; Schmid, S.M.; Ziegler, P.A. Evolution of the European Cenozoic Rift System: Interaction of the Alpine and Pyrenean Orogens with Their Foreland Lithosphere. *Tectonophysics* **2004**, *389*, 1–33. [CrossRef]
41. Bourgeois, O.; Ford, M.; Diraison, M.; de Veslud, C.L.C.; Gerbault, M.; Pik, R.; Ruby, N.; Bonnet, S. Separation of Rifting and Lithospheric Folding Signatures in the NW-Alpine Foreland. *Int. J. Earth Sci. (Geol. Rundsch.)* **2007**, *96*, 1003–1031. [CrossRef]
42. Michon, L.; Merle, O. Mode of Lithospheric Extension: Conceptual Models from Analogue Modeling. *Tectonics* **2003**, *22*, 1028. [CrossRef]
43. Michon, L.; Merle, O. Discussion on "Evolution of the European Cenozoic Rift System: Interaction of the Alpine and Pyrenean Orogens with Their Foreland Lithosphere" by P. Dèzes, S.M. Schmid and P.A. Ziegler, Tectonophysics 389 (2004) 1–33. *Tectonophysics* **2005**, *401*, 251–256. [CrossRef]
44. Ziegler, P.A.; Schumacher, M.E.; Dèzes, P.; Van Wees, J.-D.; Cloetingh, S. Post-Variscan Evolution of the Lithosphere in the Rhine Graben Area: Constraints from Subsidence Modelling. *Geol. Soc. Lond. Spec. Publ.* **2004**, *223*, 289–317. [CrossRef]
45. Schumacher, M.E. Upper Rhine Graben: Role of Preexisting Structures during Rift Evolution. *Tectonics* **2002**, *21*, 6-1–6-17. [CrossRef]
46. Ustaszewski, K.; Schumacher, M.E.; Schmid, S.M. Simultaneous Normal Faulting and Extensional Flexuring during Rifting: An Example from the Southernmost Upper Rhine Graben. *Int. J. Earth Sci. (Geol. Rundsch.)* **2005**, *94*, 680–696. [CrossRef]
47. Korsch, R.J.; Schäfer, A. Geological Interpretation of DEKORP Deep Seismic Reflection Profiles 1C and 9N across the Variscan Saar-Nahe Basin Southwest Germany. *Tectonophysics* **1991**, *191*, 127–146. [CrossRef]
48. Krohe, A. Structural Evolution of Intermediate-Crustal Rocks in a Strike-Slip and Extensional Setting (Variscan Odenwald, SW Germany): Differential Upward Transport of Metamorphic Complexes and Changing Deformation Mechanisms. *Tectonophysics* **1992**, *205*, 357–386. [CrossRef]

49. Murawski, H.; Albers, H.J.; Bender, P.; Berners, H.-P.; Dürr, S.; Huckriede, R.; Kauffmann, G.; Kowalczyk, G.; Meiburg, P.; Müller, R.; et al. Regional Tectonic Setting and Geological Structure of the Rhenish Massif. In *Plateau Uplift*; Fuchs, K., von Gehlen, K., Mälzer, H., Murawski, H., Semmel, A., Eds.; Springer: Berlin/Heidelberg, Germany, 1983; pp. 9–38. ISBN 978-3-642-69221-5.
50. Hirschmann, G. Some Remarks on the Position of the Rhenish Massif Between the Variscides and the Caledonides. In *The Rhenish Massif*; Vogel, A., Miller, H., Greiling, R., Eds.; Vieweg+Teubner Verlag: Wiesbaden, Germany, 1987; pp. 104–112. ISBN 978-3-663-01888-9.
51. Hirschmann, G. Lithological Characteristics. In *Pre-Permian Geology of Central and Eastern Europe*; Dallmeyer, R.D., Franke, W., Weber, K., Eds.; IGCP-Project 233; Springer: Berlin/Heidelberg, Germany, 1995; pp. 155–163. ISBN 978-3-642-77518-5.
52. Dörr, W.; Stein, E. Precambrian Basement in the Rheic Suture Zone of the Central European Variscides (Odenwald). *Int. J. Earth Sci. (Geol. Rundsch.)* **2019**, *108*, 1937–1957. [CrossRef]
53. Will, T.M.; Schulz, B.; Schmädicke, E. The Timing of Metamorphism in the Odenwald–Spessart Basement, Mid-German Crystalline Zone. *Int. J. Earth Sci. (Geol. Rundsch.)* **2017**, *106*, 1631–1649. [CrossRef]
54. Stein, E. The Geology of the Odenwald Crystalline Complex. *Mineral. Petrol.* **2001**, *72*, 7–28. [CrossRef]
55. Rotstein, Y.; Edel, J.-B.; Gabriel, G.; Boulanger, D.; Schaming, M.; Munschy, M. Insight into the Structure of the Upper Rhine Graben and Its Basement from a New Compilation of Bouguer Gravity. *Tectonophysics* **2006**, *425*, 55–70. [CrossRef]
56. Kirsch, H.; Kober, B.; Lippolt, H.J. Age of Intrusion and Rapid Cooling of the Frankenstein Gabbro (Odenwald, SW-Germany) Evidenced By40Ar/39Ar and Single-Zircon207Pb/206Pb Measurements. *Geol. Rundsch.* **1988**, *77*, 693–711. [CrossRef]
57. Krohe, A.; Willner, A.P. The Odenwald Crystalline Complex. In *Pre-Permian Geology of Central and Eastern Europe*; Dallmeyer, R.D., Franke, W., Weber, K., Eds.; IGCP-Project 233; Springer: Berlin, Heidelberg, 1995; pp. 174–181. ISBN 978-3-642-77518-5.
58. Altherr, R.; Henes-Klaiber, U.; Hegner, E.; Satir, M.; Langer, C. Plutonism in the Variscan Odenwald (Germany): From Subduction to Collision. *Int. J. Earth Sci.* **1999**, *88*, 422–443. [CrossRef]
59. McCann, T. *The Geology of Central Europe: Volume 1: Precambrian and Palaeozoic*; Geological Society of London: London, UK, 2008. [CrossRef]
60. Mezger, J.E.; Felder, M.; Harms, F.-J. Crystalline Rocks in the Maar Deposits of Messel: Key to Understand the Geometries of the Messel Fault Zone and Diatreme and the Post-Eruptional Development of the Basin Fill. *zdgg* **2013**, *164*, 639–662. [CrossRef] [PubMed]
61. Anderle, H.J. The Evolution of the South Hunsrück and Taunus Borderzone. *Tectonophysics* **1987**, *137*, 101–114. [CrossRef]
62. Izart, A.; Barbarand, J.; Michels, R.; Privalov, V.A. Modelling of the Thermal History of the Carboniferous Lorraine Coal Basin: Consequences for Coal Bed Methane. *Int. J. Coal Geol.* **2016**, *168*, 253–274. [CrossRef]
63. Duringer, P.; Aichholzer, C.; Orciani, S.; Genter, A. The Complete Lithostratigraphic Section of the Geothermal Wells in Rittershoffen (Upper Rhine Graben, Eastern France): A Key for Future Geothermal Wells. *BSGF-Earth Sci. Bull.* **2019**, *190*, 13. [CrossRef]
64. Liang, F.; Niu, J.; Linsel, A.; Hinderer, M.; Scheuvens, D.; Petschick, R. Rock Alteration at the Post-Variscan Nonconformity: Implications for Carboniferous–Permian Surface Weathering versus Burial Diagenesis and Paleoclimate Evaluation. *Solid Earth* **2021**, *12*, 1165–1184. [CrossRef]
65. Edel, J.B.; Schneider, J.L. The Late Carboniferous to Early Triassic Geodynamic Evolution of Variscan Europe in the Light of Magnetic Overprints in Early Permian Rhyolites from the Northern Vosges (France) and Central Black Forest (Germany). *Geophys. J. Int.* **1995**, *122*, 858–876. [CrossRef]
66. McCann, T.; Pascal, C.; Timmerman, M.J.; Krzywiec, P.; López-Gómez, J.; Wetzel, L.; Krawczyk, C.M.; Rieke, H.; Lamarche, J. Post-Variscan (End Carboniferous-Early Permian) Basin Evolution in Western and Central Europe. *Geol. Soc. Lond. Mem.* **2006**, *32*, 355–388. [CrossRef]
67. Böcker, J.; Littke, R. Thermal Maturity and Petroleum Kitchen Areas of Liassic Black Shales (Lower Jurassic) in the Central Upper Rhine Graben, Germany. *Int. J. Earth Sci. (Geol. Rundsch.)* **2016**, *105*, 611–636. [CrossRef]
68. Böcker, J.; Littke, R.; Forster, A. An Overview on Source Rocks and the Petroleum System of the Central Upper Rhine Graben. *Int. J. Earth Sci. (Geol. Rundsch.)* **2017**, *106*, 707–742. [CrossRef]
69. Meulenkamp, J.E.; Sissingh, W. Tertiary Palaeogeography and Tectonostratigraphic Evolution of the Northern and Southern Peri-Tethys Platforms and the Intermediate Domains of the African–Eurasian Convergent Plate Boundary Zone. *Palaeogeogr. Palaeoclimatol. Palaeoecol.* **2003**, *196*, 209–228. [CrossRef]
70. Sissingh, W. Tectonostratigraphy of the North Alpine Foreland Basin: Correlation of Tertiary Depositional Cycles and Orogenic Phases. *Tectonophysics* **1997**, *282*, 223–256. [CrossRef]
71. Ford, M.; Le Carlier de Veslud, C.; Bourgeois, O. Kinematic and Geometric Analysis of Fault-Related Folds in a Rift Setting: The Dannemarie Basin, Upper Rhine Graben, France. *J. Struct. Geol.* **2007**, *29*, 1811–1830. [CrossRef]
72. Ziegler, P.A.; Dèzes, P. Cenozoic Uplift of Variscan Massifs in the Alpine Foreland: Timing and Controlling Mechanisms. *Glob. Planet. Chang.* **2007**, *58*, 237–269. [CrossRef]
73. Derer, C.E.; Schumacher, M.E.; Schäfer, A. The Northern Upper Rhine Graben: Basin Geometry and Early Syn-Rift Tectono-Sedimentary Evolution. *Int. J. Earth Sci. (Geol. Rundsch.)* **2005**, *94*, 640–656. [CrossRef]
74. Meixner, J.; Schill, E.; Grimmer, J.C.; Gaucher, E.; Kohl, T.; Klingler, P. Structural Control of Geothermal Reservoirs in Extensional Tectonic Settings: An Example from the Upper Rhine Graben. *J. Struct. Geol.* **2016**, *82*, 1–15. [CrossRef]

75. Rotstein, Y.; Schaming, M.; Rousse, S. Tertiary Tectonics of the Dannemarie Basin, Upper Rhine Graben, and Regional Implications. *Int. J. Earth Sci. (Geol. Rundsch.)* **2005**, *94*, 669–679. [CrossRef]
76. Lutz, H.; Kaulfuss, U.; Wappler, T.; Löhnertz, W.; Wilde, V.; Mertz, D.F.; Mingram, J.; Franzen, J.L.; Frankenhäuser, H.; Koziol, M. Eckfeld Maar: Window into an Eocene Terrestrial Habitat in Central Europe. *Acta Geol. Sin.—Engl. Ed.* **2010**, *84*, 984–1009. [CrossRef]
77. Lutz, H.; Lorenz, V.; Engel, T.; Häfner, F.; Haneke, J. Paleogene Phreatomagmatic Volcanism on the Western Main Fault of the Northern Upper Rhine Graben (Kisselwörth Diatreme and Nierstein–Astheim Volcanic System, Germany). *Bull. Volcanol.* **2013**, *75*, 741. [CrossRef]
78. Krohe, A. Emplacement of Synkinematic Plutons in the Variscan Odenwald (Germany) Controlled by Transtensional Tectonics. *Geol. Rundsch.* **1991**, *80*, 391–409. [CrossRef]
79. Thews, J.-D. *Erläuterungen Zur Geologischen Übersichtskarte von Hessen 1:300000 (GÜK300 Hessen) Teil I: Kristallin, Ordoviz, Silur, Devon, Karbon.-Geologische Abhandlungen von Hessen, Bd. 96, 1996*; Hessisches Landesamt Für Umwelt Und Geologie: Wiesbaden, Germany, 1996.
80. Heidbach, O.; Rajabi, M.; Cui, X.; Fuchs, K.; Müller, B.; Reinecker, J.; Reiter, K.; Tingay, M.; Wenzel, F.; Xie, F.; et al. The World Stress Map Database Release 2016: Crustal Stress Pattern across Scales. *Tectonophysics* **2018**, *744*, 484–498. [CrossRef]
81. Bossennec, C.; Frey, M.; Seib, L.; Bär, K.; Sass, I. *Multi-Scale Structural Dataset of a Crystalline Reservoir Analogue (Northern Odenwald)*; TUdatalib: Darmstadt, Germany, 2021.
82. Frey, M.; Bossennec, C.; Seib, L.; Bär, K.; Sass, I. *Interdisciplinary Dataset on the Fracture Network of the Tromm Granite, Southern Odenwald, SW Germany*; TUdatalib: Darmstadt, Germany, 2021.
83. Schnabel, R.; Wahl, R.; Klein, R. Efficient RANSAC for Point-Cloud Shape Detection. *Comput. Graph. Forum* **2007**, *26*, 214–226. [CrossRef]
84. SAGA Tool Library Documentation. Available online: http://www.saga-gis.org/saga_tool_doc/ (accessed on 27 September 2021).
85. Ghosh, K.; Mitra, S. Structural Controls of Fracture Orientations, Intensity, and Connectivity, Teton Anticline, Sawtooth Range, Montana. *Bulletin* **2009**, *93*, 995–1014. [CrossRef]
86. Ortega, O.J.; Marrett, R.A.; Laubach, S.E. A Scale-Independent Approach to Fracture Intensity and Average Spacing Measurement. *Bulletin* **2006**, *90*, 193–208. [CrossRef]
87. Primaleon, L.P.; McCaffrey, K.J.W.; Holdsworth, R.E. Fracture Attribute and Topology Characteristics of a Geothermal Reservoir: Southern Negros, Philippines. *J. Geol. Soc.* **2020**, *177*, 1092–1106. [CrossRef]
88. Sanderson, D.J.; Nixon, C.W. The Use of Topology in Fracture Network Characterization. *J. Struct. Geol.* **2015**, *72*, 55–66. [CrossRef]
89. Outters, N. *A Generic Study of Discrete Fracture Network Transport Properties Using FracMan/MAFIC*; Swedish Nuclear Fuel and Waste Management Co.: Stockholm, Sweden, 2003.
90. Lee, C.-C.; Lee, C.-H.; Yeh, H.-F.; Lin, H.-I. Modeling Spatial Fracture Intensity as a Control on Flow in Fractured Rock. *Environ. Earth Sci.* **2011**, *63*, 1199–1211. [CrossRef]
91. Kemeny, J.; Post, R. Estimating Three-Dimensional Rock Discontinuity Orientation from Digital Images of Fracture Traces. *Comput. Geosci.* **2003**, *29*, 65–77. [CrossRef]
92. Ahlers, S.; Henk, A.; Hergert, T.; Reiter, K.; Müller, B.; Röckel, L.; Heidbach, O.; Morawietz, S.; Scheck-Wenderoth, M.; Anikiev, D. 3D Crustal Stress State of Germany According to a Data-Calibrated Geomechanical Model. *Solid Earth* **2021**, *12*, 1777–1799. [CrossRef]
93. Lanaro, F.; Fredriksson, A. *Rock Mechanics Model—Summary of the Primary Data—Preliminary Site Description—Forsmark Area—Version 1.2. 41*; Swedish Nuclear Fuel and Waste Management Co.: Stockholm, Sweden, 2005.
94. Andrianov, N.; Nick, H.M. Modeling of Waterflood Efficiency Using Outcrop-Based Fractured Models. *J. Pet. Sci. Eng.* **2019**, *183*, 106350. [CrossRef]
95. Lawn, B. *Fracture of Brittle Solids*; Cambridge Solid State Science Series; Cambridge University Press: London, UK, 1993.
96. Klimczak, C.; Schultz, R.A.; Parashar, R.; Reeves, D.M. Cubic Law with Aperture-Length Correlation: Implications for Network Scale Fluid Flow. *Hydrogeol. J.* **2010**, *18*, 851–862. [CrossRef]
97. Oda, M. Permeability Tensor for Discontinuous Rock Masses. *Géotechnique* **1985**, *35*, 483–495. [CrossRef]
98. Chiles, J.-P.; Delfiner, P. *Geostatistics: Modeling Spatial Uncertainty*; Wiley Series in Probability and Statistics; Wiley: Hoboken, NJ, USA, 1999.
99. Abrahamsen, P.; Hauge, R.; Kolbjørnsen, O. *Geostatistics Oslo 2012*; Springer Science & Business Media: Berlin/Heidelberg, Germany, 2012; ISBN 978-94-007-4153-9.
100. Wellmann, J.F.; Horowitz, F.G.; Schill, E.; Regenauer-Lieb, K. Towards Incorporating Uncertainty of Structural Data in 3D Geological Inversion. *Tectonophysics* **2010**, *490*, 141–151. [CrossRef]
101. Chabani, A.; Trullenque, G.; Ledésert, B.A.; Klee, J. Multiscale Characterization of Fracture Patterns: A Case Study of the Noble Hills Range (Death Valley, CA, USA), Application to Geothermal Reservoirs. *Geosciences* **2021**, *11*, 280. [CrossRef]
102. Greiling, R.O.; Verma, P.K. Strike-Slip and Tectonics Granitoid Emplacement: An AMS Fabric Study from the Odenwald Crystalline Complex, SW Germany. *Mineral. Petrol.* **2001**, *72*, 165–184. [CrossRef]

103. Meixner, J.; Grimmer, J.C.; Becker, A.; Schill, E.; Kohl, T. Comparison of Different Digital Elevation Models and Satellite Imagery for Lineament Analysis: Implications for Identification and Spatial Arrangement of Fault Zones in Crystalline Basement Rocks of the Southern Black Forest (Germany). *J. Struct. Geol.* **2018**, *108*, 256–268. [CrossRef]
104. Egert, R.; Korzani, M.G.; Held, S.; Kohl, T. Implications on Large-Scale Flow of the Fractured EGS Reservoir Soultz Inferred from Hydraulic Data and Tracer Experiments. *Geothermics* **2020**, *84*, 101749. [CrossRef]
105. Mahmoodpour, S.; Singh, M.; Turan, A.; Bär, K.; Sass, I. Hydro-Thermal Modeling for Geothermal Energy Extraction from Soultz-Sous-Forêts, France. *Geosciences* **2021**, *11*, 464. [CrossRef]
106. Sausse, J. Hydromechanical Properties and Alteration of Natural Fracture Surfaces in the Soultz Granite (Bas-Rhin, France). *Tectonophysics* **2002**, *348*, 169–185. [CrossRef]
107. Bonneau, F.; Henrion, V.; Caumon, G.; Renard, P.; Sausse, J. A Methodology for Pseudo-Genetic Stochastic Modeling of Discrete Fracture Networks. *Comput. Geosci.* **2013**, *56*, 12–22. [CrossRef]
108. Lepillier, B.; Daniilidis, A.; Doonechaly Gholizadeh, N.; Bruna, P.-O.; Kummerow, J.; Bruhn, D. A Fracture Flow Permeability and Stress Dependency Simulation Applied to Multi-Reservoirs, Multi-Production Scenarios Analysis. *Geotherm. Energy* **2019**, *7*, 24. [CrossRef]
109. Bruna, P.-O.; Straubhaar, J.; Prabhakaran, R.; Bertotti, G.; Bisdom, K.; Mariethoz, G.; Meda, M. A New Methodology to Train Fracture Network Simulation Using Multiple-Point Statistics. *Solid Earth* **2019**, *10*, 537–559. [CrossRef]
110. Sahu, A.; Roy, A. Evaluating Flow in Fractal-Fracture Networks: Effect of Variable Aperture. *Adv. Geosci.* **2021**, *56*, 117–128. [CrossRef]
111. Sanderson, D.J.; Peacock, D.C.P. Line Sampling of Fracture Swarms and Corridors. *J. Struct. Geol.* **2019**, *122*, 27–37. [CrossRef]
112. Peacock, D.C.; Sanderson, D.J.; Bastesen, E.; Rotevatn, A.; Storstein, T.H. Causes of Bias and Uncertainty in Fracture Network Analysis. *Nor. J. Geol.* **2019**, *99*, 113–128. [CrossRef]
113. Ngoc, N.H.; Aziz, S.B.; Duc, N.A. The Application of Seismic Attributes for Reservoir Characterization in Pre-Tertiary Fractured Basement, Vietnam-Malaysia Offshore. *Interpretation* **2014**, *2*, SA57–SA66. [CrossRef]
114. Mahmoodpour, S.; Singh, M.; Bär, K.; Sass, I. Impact of Well Placement in the Fractured Geothermal Reservoirs Based on Available Discrete Fractured System. *Geosciences* **2022**, *12*, 19. [CrossRef]
115. Calò, M.; Dorbath, C.; Frogneux, M. Injection Tests at the EGS Reservoir of Soultz-Sous-Forêts. Seismic Response of the GPK4 Stimulations. *Geothermics* **2014**, *52*, 50–58. [CrossRef]
116. Schmittbuhl, J.; Lengliné, O.; Cornet, F.; Cuenot, N.; Genter, A. Induced Seismicity in EGS Reservoir: The Creep Route. *Geothermal Energy* **2014**, *2*, 14. [CrossRef]
117. Zang, A.; Oye, V.; Jousset, P.; Deichmann, N.; Gritto, R.; McGarr, A.; Majer, E.; Bruhn, D. Analysis of Induced Seismicity in Geothermal Reservoirs—An Overview. *Geothermics* **2014**, *52*, 6–21. [CrossRef]